

A MULTIGRID METHOD FOR TWO AND
THREE-DIMENSIONAL FLOWS
BEHIND BLUFF BODIES IN A CHANNEL

*A Thesis Submitted
in Partial Fulfillment of the Requirements
for the Degree of*

MASTER OF TECHNOLOGY

210811

by

ARUN KUMAR SAHA

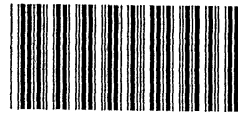
to the

DEPARTMENT OF MECHANICAL ENGINEERING
INDIAN INSTITUTE OF TECHNOLOGY
KANPUR

JUNE, 1994

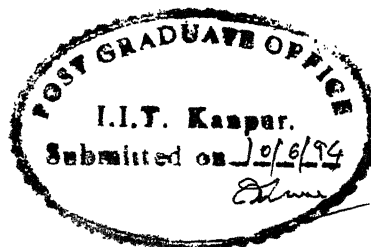
70
552.54
Sa 19m

6 JUL 1994/ME
CENTRAL LIBRARY
402. No. A. **118019**



A118019

ME-1994-M-SAH-MUL



CERTIFICATE

This is to certify that the thesis entitled **A Multigrid Method for Two and Three-Dimensional Flows Behind Bluff Bodies in a Channel**, by *Arun Kumar Saha* has been carried out under my supervision and that this work has not been submitted elsewhere for a degree.

June, 1994

Gautam Biswas
(Dr. G. Biswas)

Associate Professor
Dept. of Mechanical Engineering
Indian Institute of Technology
Kanpur 208016

A Multigrid Method for Two and Three-Dimensional Flows Behind Bluff Bodies in a Channel

Abstract

An investigation has been undertaken on the possibility of increasing speed of convergence of a existing computer code for the simulation of flow past bluff bodies in a channel. A multigrid method has been developed for the pressure-velocity iteration of the Marker and Cell (MAC) method used for the solution of full Navier-Stokes equations. For flows with complex configuration a remarkable reduction of computational time has been observed in a single V-cycle vis-a-vis single grid computations. The multigrid technique is based on the strategy that the low frequency errors of one grid can be solved on a coarser grid at the high frequency rate. The finer grid solution can then be corrected for the low frequency errors. The flow simulations using the multigrid scheme compare well with the single grid and available experimental results.

Acknowledgements

I deeply express my sincere thanks, whole hearted regards and gratitude to my supervisor Dr. Gautam Biswas who inspired and guided me with deep interest.

A note of thanks and gratitude is due also to Dr. T. Sundararajan who took interest in my work.

I am also indebted to Anshul Gupta, Chetan Kumar and P. Deb for their help and encouragement.

I would like to record my thanks to my colleagues R. Dutta and B. Ghosh for their company during my stay at IIT, Kanpur.

Finally, I appreciate the help and inspiration received from my family-members and well-wishers.

Arun Kumar Saha

Contents

1	Introduction	1
1.1	Background of the Problem	1
1.2	Review of Literature	2
1.3	Scope of the Work	6
1.4	Organisation of the Thesis	7
2	Mathematical Modelling of Flow Problem	8
2.1	Introduction	8
2.2	Effect of Blockage Ratio, Reynolds Number and Neighbouring walls on Vortex Shedding	10
2.3	Governing Equations and Boundary Conditions	10
2.4	Boundary Conditions	11
2.5	Grid System Used	12
2.6	Numerical Boundary Conditions	13
2.6.1	Boundary Conditions for Confining Walls	13

2.6.2	Boundary Conditions for the Obstacle	15
2.7	Closure	16
3	Solution Procedure	18
3.1	Solution Algorithm	18
3.2	Details of the Computational scheme	18
3.3	Discretization of Governing Differential Equation	19
3.4	Pressure-Velocity Iteration	20
3.5	Stability Criteria	23
4	Multigrid Implementation	25
4.1	Objective	25
4.2	Grid Arrangement	27
4.3	Multigrid Strategy	29
4.3.1	Restriction	29
4.3.2	Prolongation	33
4.3.3	Velocity Boundary Conditions for Multigrid	36
4.4	Closure	36
5	Results and Discussions	37
5.1	Flow Simulation	37
5.1.1	Two-Dimensional Flow in a Channel With a Built-in Square Cylinder	37

5.1.2	Three-Dimensional Flow in a Channel With Built-in Square Cylinder	44
5.2	Computational Aspects of the Multigrid Technique	48
5.2.1	Two-Dimensional Case	48
5.2.2	Three-Dimensional Case	50
6	Concluding Remarks	52

List of Figures

1.1	Error spectrum	3
1.2	Typical error smoothing behaviour of appropriate relaxation method . . .	4
2.1	Flow models for computation, (a) two-dimension, (b) three-dimension . .	9
2.2	Discretization of a three-dimensional domain	12
2.3	Three-dimensional staggered grid showing the locations of the discretized variables	13
2.4	Boundary conditions and fictitious boundary cells	15
2.5	Discretization of the three-dimensional square obstacle	16
4.1	Computational sequence of the MAC algorithm	26
4.2	Three different grid levels for a multigrid technique	28
4.3	A V - cycle (CS mode)	30
4.4	Restriction of residuals (defects) to coarse grid	30
4.5	Fine- and coarse-grid values of restriction	32
4.6	Interpolation of coarse grid pressure corrections to finer grid	35
5.1	Attached vortices behind the obstacle at $Re_B = 40$	38

5.2	Attached vortices behind the obstacle at $Re_B = 60$	39
5.3	(a) The wake is beginning to shed vortices into the stream, $Re_B = 80$ (b) Magnified view of the wake immediate behind the obstacle	40
5.4	Velocity vectors in the channel at different nondimensional time, ($Re_B = 250$) (a) $\tau = 5.0823$ (b) $\tau = 7.4676$	41
5.5	Streamline crossing the cylinder in the channel, ($Re_B = 375$)	42
5.6	Time evolution of lift coefficient for (a) $Re_B = 250$ (b) $Re_B = 375$	45
5.7	Streaklines in a channel with built-in square cylinder, $Re_B = 150$	46

List of Tables

5.1	Variation of Strouhal number with Reynolds number	43
5.2	Comparison of present computation with experimental (Okajima, 1982) results	47
5.3	Comparison of CPU-times and Workunits between the multigrid and single- grid for two-dimensional problem	49
5.4	Comparison of Workunits between the multigrid and single-grid for the three-dimensional problem	50

Nomenclature

B	obstacle width
D	channel width
H	channel height
L	characteristic length
t	time
D	divergence of velocity vectors
p	static pressure
P	nondimensional static pressure, $p/\rho U_{av}^2$
\tilde{P}	pressure distribution on the square prism surface
Re	Reynolds number based on channel height, $\rho U_{av} H / \mu$
Re_B	Reynolds number based on obstacle width, $\rho U_{av} B / \mu$
x, y, z	axial, vertical or normal, and spanwise dimension of coordinates
X, Y, Z	axial, vertical or normal, and spanwise coordinates (normalized by H)
u, v, w	axial, vertical, spanwise components of velocity
U, V, W	axial, vertical, spanwise components of laminar velocity (nondimensional)
h	grid size
C_L	lift coefficient, $\mathcal{L}/(\frac{1}{2}\rho U_{av}^2 A)$
\mathcal{L}	lift force on the square prism, $\sum \tilde{P}_1 \delta X - \sum \tilde{P}_2 \delta X$

S Strouhal number, fB/U_{av}

T time period of oscillation, $1/f$

f frequency of vortex shedding

Greek symbols

α_p upwinding factor

μ dynamic viscosity of the fluid

ν numbers of relaxation sweeps on pressure-velocity equation

τ nondimensional time, $t/(H/U_{av})$

ρ density of the fluid

ω_s relaxation factor

Subscripts

av average

nb neighbouring values

l grid level

m mid-plane

Chapter 1

Introduction

1.1 Background of the Problem

A multigrid technique has been implemented to accelerate the convergence of the solution of flow equations in a complex configuration. The flow in a channel with built-in square obstacle has been presented as a test problem for implementation of the multigrid technique.

Fluid mechanics is an all pervasive subject. Application of fluid mechanics are numerous to list. In engineering, almost every equipment has some components that need to be cooled, heated, lubricated or supplied with energy. So, design of these components requires the knowledge of detailed velocity, temperature and pressure fields. Only detailed knowledge can lead to improved designs, low maintenance cost and reduced pollution *etc..* Experiments can also give the detailed information about these parameters but the difficulties are with (i) cost, (ii) safety, (iii) feasibility and (iv) time.

Predictive procedure is one of the solutions of eliminating these difficulties. But accuracy of a predictive procedure is very much dependent on the number of grids in the domain. If the number of grids are increased considerably, the computation becomes costly and obviously, the calculations take enormous time. In order to circumvent the reduced computational speed, the multigrid techniques are suggested. It is conjectured that the multigrid techniques will accelerate the computational speed well above the

computational time due to single-grid codes.

In the present work, the flow in a channel with built-in obstacles is simulated by solving the full Navier-Stokes equations for incompressible viscous flows. The determination of the dominating frequency in flow induced vibration with moderate Reynolds number is the main concern while designing big structures which are susceptible to oscillations. The present study provides a fast flow-solver algorithm for determining the dominating frequency for such structures.

1.2 Review of Literature

Despite substantial progress in both hardware and software the computational fluid dynamics calculations need higher computational speed. Highly accurate flow-physics simulations clearly require enormous number of points in the computational domain which slows down the convergence. A question arises whether improvements in numerical techniques can be expected to show somewhat increasing convergence rate for a given accuracy.

The sequential scalar processors used in present-day hardware may be referred to as being single-instruction, single-data (SISD) architecture. The technological limits for performance enhancement of SISD are approaching rapidly. Vector processors use single-instruction, multiple data (SIMD) architecture to perform a single operation simultaneously on a collection of operands. Parallel processors use multiple-instruction, multiple-data (MIMD) architecture to perform simultaneously several distinct operations, with each operation accessing its own collection of operands.

Together with the hardware improvement, one notable trend in fluid dynamics algorithm design has been the evolution of efficient algorithmic improvements, such as, domain decomposition and multigrid techniques. The multigrid method is indeed capable of accelerating the speed of computation. The multigrid algorithms have been well documented by Brandt (1984) and Stüben and Trottenberg (1982). Multigridging is used to designate a process that carries a residual through a series of operations in order to accelerate the removal of error from the solution. The operations are related to the

grid size, which becomes increasingly coarse during one part of the iteration (operation) and increasingly fine during the other.

It is a common phenomenon in any type of relaxation scheme that after first five or six iterations the convergence rate slows down. The rate of convergence strongly depends on the mesh size. It becomes slower as the mesh is refined. At any stage of relaxation the error spectrum will contain a number of discrete frequencies, represented by Fourier components as shown in Fig.1.1.

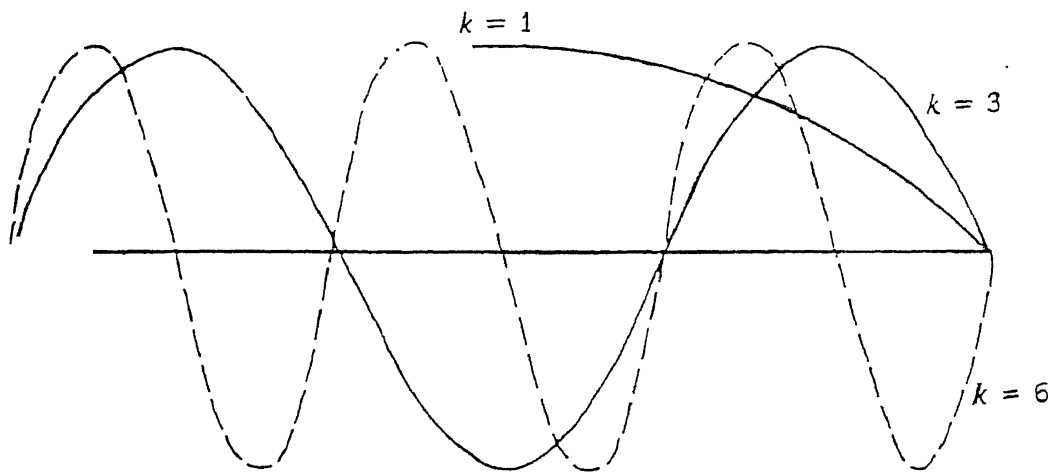
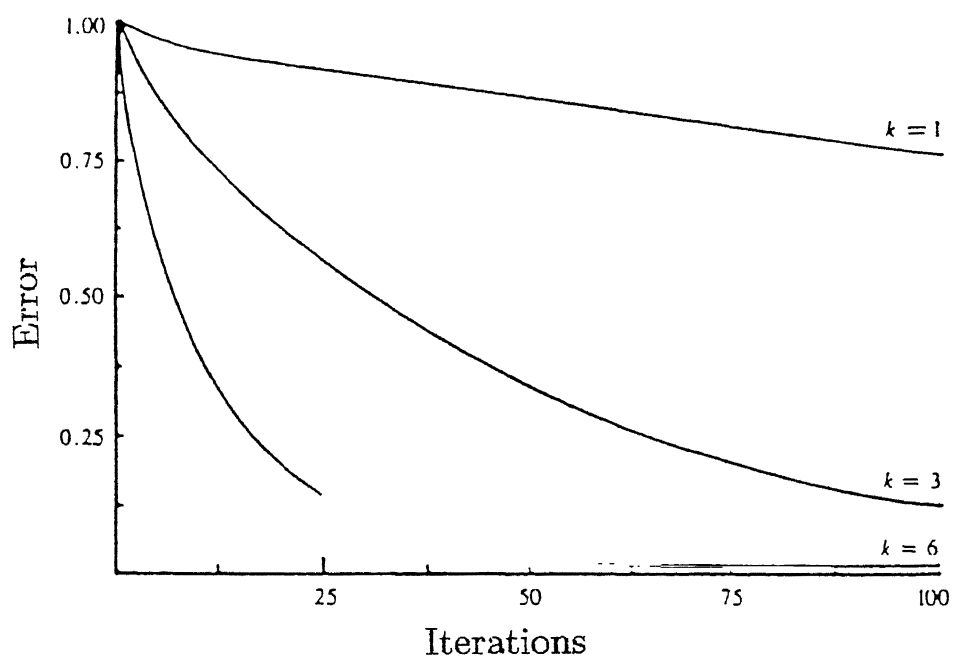


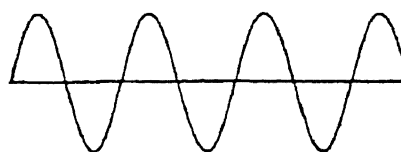
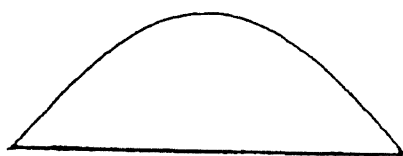
Figure 1.1: Error spectrum

Each frequency converges at a different rate. The high frequencies converge the fastest and the low frequencies the slowest. So, the convergence is held up by the longer wavelength or the low frequency components of the error spectrum. The nature of error elimination for different frequencies are shown in Figures 1.2(a) and 1.2(b). Each iterative procedure has different rates of convergence (smoothing rates) for each range of frequency. Out of the different methods of iterative (relaxation) procedures, Gauss-Seidel is the cheapest in workcount, but the convergence rate for low frequencies is slow.

It is known from previous discussion that the low and high frequency demarcation



(a)

Low frequencies:High frequencies:Before relaxationAfter relaxationSlight reduction of the amplitudeSignificant reduction of the amplitude

(b)

Figure 1.2: Typical error smoothing behaviour of appropriate relaxation method

is a function of the grid. That is, the low frequencies on one fine grid can become high frequencies on a coarser grid. In multigrid technique, several grid levels are generated. Each grid level can be constructed by halving the fine grid or by doubling the coarse grid. It is easy to have grids of increasing fineness if one starts from coarsest grid. So, after generating all the grid levels, the errors in the solution are resolved efficiently by using these grids in a continuous cycling procedure.

As a summary, it can be stated that the multigrid technique uses the following steps :

1. Detecting the high and low frequencies.
2. Resolving the high frequencies.
3. Calculating the low frequency components.
4. Transferring the residuals or defects to coarser grids.
5. Solving the equations on coarser grids.
6. Transferring the corrections back to finer grids.

A large amount of literature (Brandt, 1984; Stüben and Trottenburg, 1982; Ghia *et al*, 1982; Brockmeier *et al*, 1986; Vanka, 1986a) exists on the theory and performance of the multigrids on model equations. However, despite its potential, a few investigations have been reported in which practically important viscous flows have been computed with the help of multigrid technique. A few researchers reported about the investigations of the driven cavity problem (Ghia *et al*, 1982; Agarwal, 1981; Philips and Schmidt, 1985) in which the stream function and vorticity equations (Ghia *et al* , 1982 and Agarwal, 1981) and the primitive variable equations (Philips and Schmidt, 1985) are solved. Applications of multigrid technique to a sudden-expansion flow (Philips *et al* , 1985) and a three dimensional duct flow (Fuch and Zhao, 1984) have recently been reported. Multigrid solution of the Euler equations have been reported, by Jameson and coworkers (1983) and by Chima and Johnson (1985). However, many practical viscous flows (such as those in combustors, turbomachinery, heat exchangers, *etc.*) are currently being solved by single-grid techniques. The application of the multigrid technique to accelerate

the convergence of these calculations remains to be explored. In recent works of Vanka (1986a & 1986c), a calculation procedure based on a coupled simultaneous relaxation of the momentum and continuity equations was successfully used in association with the multigrid technique to analyse the complex flow fields in shear-driven square and cubic cavities. The relaxation procedure used in cavity problems is called Symmetrical Coupled Gauss-Seidel (SCGS) and by this procedure the equations are solved node by node in a coupled manner. At each node, the four (or six) velocities located on the cell faces and the pressure are simultaneously updated by the coupled solution of the relevant momentum and continuity equations. Such a coupled relaxation is advocated on the basis of earlier works (Vanka, 1985 & 1986d; Galpin, 1985; Zedan and Schneider ,1985) that in internal flows, where the pressure field plays an important role in flow distribution, the rate of convergence is significantly improved when the momentum and continuity equations are relaxed simultaneously. In another investigation of Vanka (1986b), the performance of the above mentioned multigrid technique is assessed in four various complex configuration of recirculating flows important for industrial applications. The procedure is observed to converge rapidly to an acceptable accuracy in all the flow situations.

1.3 Scope of the Work

The objective of the present study has been to study the convergence properties of the multigrid strategy in complex flows, representative of those in many practical situations. The multigrid technique has been introduced only in the pressure-velocity (continuity) equation to get a faster convergence of correct pressure fields. This is the main condition to be fulfilled for obtaining divergence free flow fields. The multigrid algorithm has been tested through a test problem which has established single grid results. Single-grid results with respect to the vortex-shedding and wake-zone aerodynamics have been compared favourably with the multigrid results.

1.4 Organisation of the Thesis

Chapter-1 of the thesis provides the introduction of the problem and a review of literature relevant to the basic multigrid theory with brief information about the scope of the work. The mathematical modelling of flow problem for numerical simulation has been presented in Chapter-2. Chapter-3 details the solution procedure to obtain the results. Implementation of the multigrid strategy has been discussed in Chapter-4. The numerical results has been presented in Chapter-5. Comparison of performance of the multigrid and single-grid has been accomplished in this chapter. The concluding remarks with scope of further research has been mentioned in Chapter-6.

Chapter 2

Mathematical Modelling of Flow Problem

2.1 Introduction

The oscillation that we generally encounter in chimney stacks and other vertical structures in transverse flows is caused basically by vortex shedding. An initially smooth and steady flow across bluff bodies such as square cylinder, circular cylinder *etc.* may bring about the damaging deflection of the body in cases where the natural frequency of the obstacles are very close to the shedding frequency of the vortices. If the wake region behind the obstacle where Kármán vortex street has been formed, is observed carefully it will be seen that the wake zone undulates like a flag from side to side. Due to these alternating deflections of the wake, periodicity is induced in the entire flow field behind the obstacle. As a consequence of this periodicity the forces on the bluff body become periodic in nature and finally set the obstacle in vibration. If the excitation frequency of the force synchronizes with the natural frequency of the bluff body, the phenomenon of resonance will take place. Hence the study of unsteady flows across the bluff bodies have its relevance to design of structures, road vehicles, heat exchangers and wherever there is a possibility of flow induced vibration.

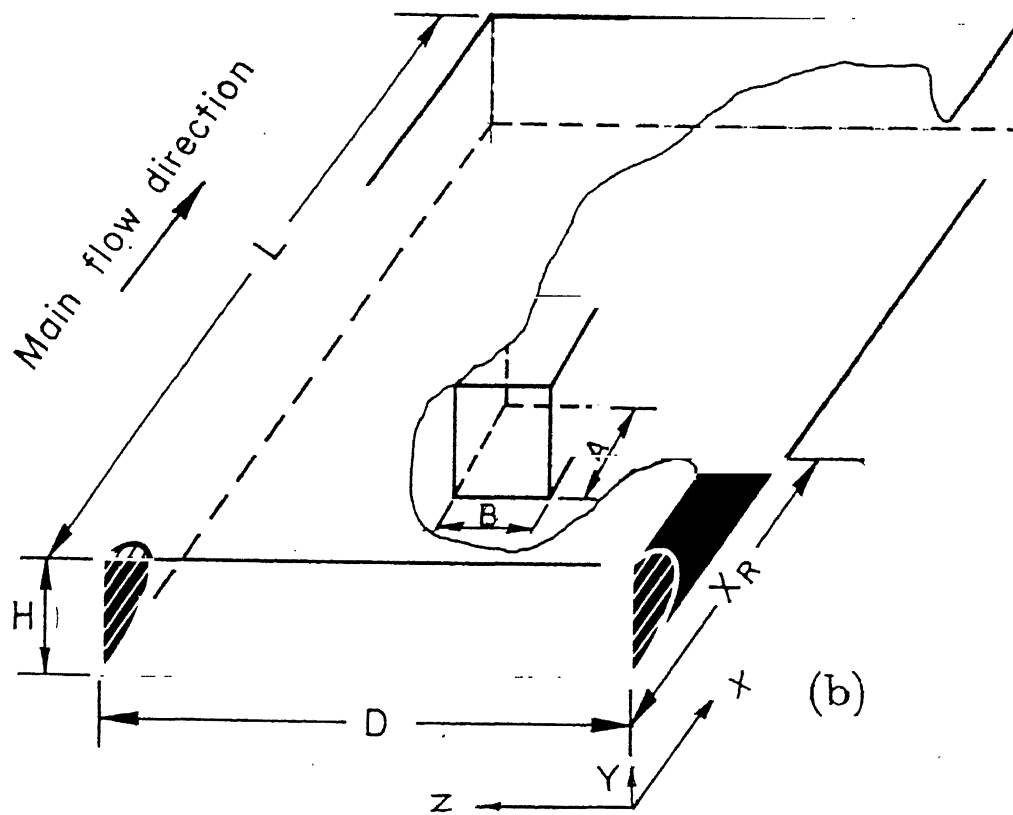
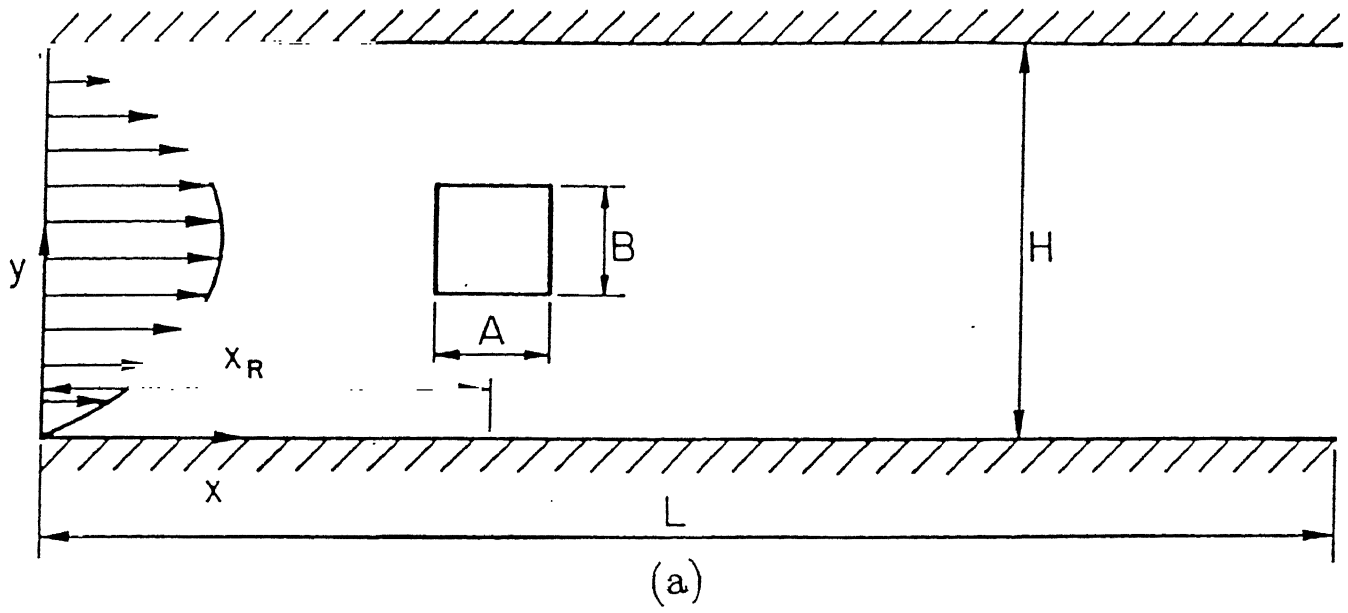


Figure 2.1: Flow models for computation, (a) two-dimension, (b) three-dimension

2.2 Effect of Blockage Ratio, Reynolds Number and Neighbouring walls on Vortex Shedding

Effect of various parameters on vortex shedding can be explained on the basis of the numerical investigation by Kiehlm, Mitra and Fiebig (1986). They explained the solutions of the two and three dimensional Navier-Stokes and continuity equations for unsteady incompressible laminar flows behind a circular cylinder in a channel of rectangular cross-section at different Reynolds numbers and blockage ratios. Their investigations on two-dimensional flow show that the periodicity of the wake becomes apparent at higher Reynolds number with lower ratios of channel width H to cylinder diameter D , *viz.*, at $Re_D = 53$ for $H/D = 5$, and at $Re_D = 170$ for $H/D = 2$. The channel walls show damping effects on the periodicity and a parabolic flow profile evolves at the exit of a long channel. From their investigation, it can be concluded that neighbouring walls always provide a damping effect on the vortex shedding behind a bluff body. For a particular blockage ratio, the amplitude of periodicity increases with increase in Reynolds number. On the other hand, critical Reynolds number for vortex shedding increases with increase in blockage ratio.

2.3 Governing Equations and Boundary Conditions

In order to have quantitative information on the flow field in a channel with a built-in square obstacle and to get their dependence on various governing parameters, numerical simulation has been carried out. The geometry of the present problem is presented in Figures 2.1(a) and 2.1(b).

The flow is simulated by solving unsteady Navier-Stokes equations for laminar, incompressible, two and three dimensional flows. The nondimensional equations for continuity and momentum for laminar incompressible flow may be expressed in their weak conservative forms as follows:

$$D \equiv \frac{\partial U}{\partial X} + \frac{\partial V}{\partial Y} + \frac{\partial W}{\partial Z} = 0 \quad (2.1)$$

$$\frac{\partial U}{\partial \tau} + \frac{\partial U^2}{\partial X} + \frac{\partial UV}{\partial Y} + \frac{\partial UW}{\partial Z} = -\frac{\partial P}{\partial X} + \frac{\nabla^2 U}{Re} \quad (2.2)$$

$$\frac{\partial V}{\partial \tau} + \frac{\partial VU}{\partial X} + \frac{\partial V^2}{\partial Y} + \frac{\partial VW}{\partial Z} = -\frac{\partial P}{\partial Y} + \frac{\nabla^2 V}{Re} \quad (2.3)$$

$$\frac{\partial W}{\partial \tau} + \frac{\partial UW}{\partial X} + \frac{\partial VW}{\partial Y} + \frac{\partial W^2}{\partial Z} = -\frac{\partial P}{\partial Z} + \frac{\nabla^2 W}{Re} \quad (2.4)$$

In the above equations the velocities are nondimensionalized with the average incoming velocity U_{av} at the inlet, all lengths with the channel height H and the pressure with ρU_{av}^2 . Reynolds number is denoted by Re .

2.4 Boundary Conditions

The boundary conditions of interest in the investigation are

- Top and bottom plates:

$$U = V = W = 0 ;$$

- side plates:

$$U = V = W = 0 ;$$

- Channel Inlet:

$$U = U(Y) , \quad V = W = 0 ;$$

- Channel Exit :

There is no unique prescription for outflow conditions. The idea is to have such conditions which do not affect the flow in the upstream. The second or higher order derivatives of all the velocity components in the streamwise direction are put to zero.

$$\frac{\partial^2 U}{\partial X^2} = \frac{\partial^2 V}{\partial X^2} = \frac{\partial^2 W}{\partial X^2} = 0 \quad (2.5)$$

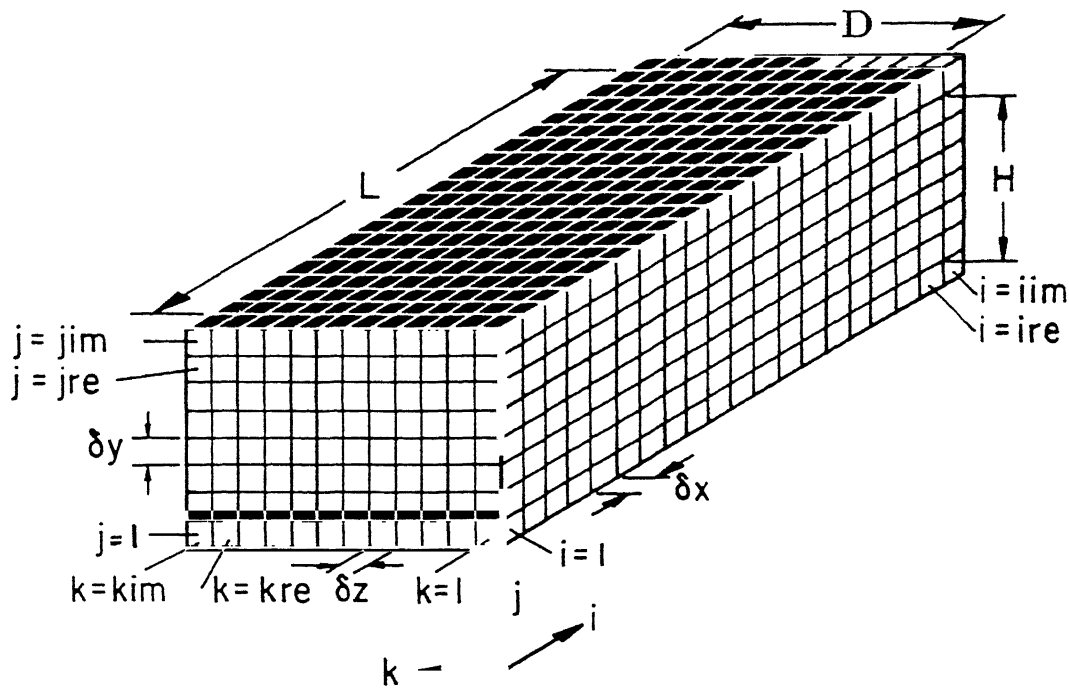


Figure 2.2: Discretization of a three-dimensional domain

- Obstacle :

No-slip boundary conditions are used for the velocities on the obstacle.

2.5 Grid System Used

For single grid system, computational domain is divided into a set of rectangular cells (Fig.2.2) and staggered grid arrangement (Fig.2.3) is used in which velocity components (vector quantities) are defined at the centre of the cell faces to which they are normal. The pressure and the divergence (scalar quantities) are defined at the cell centre. The advantages of the staggered grids are :

- pressure difference between two adjacent cells is the driving force for the velocity components located between the interface of these cells.
- transport rates across the faces of the control volume can be computed without interpolation of velocity components.

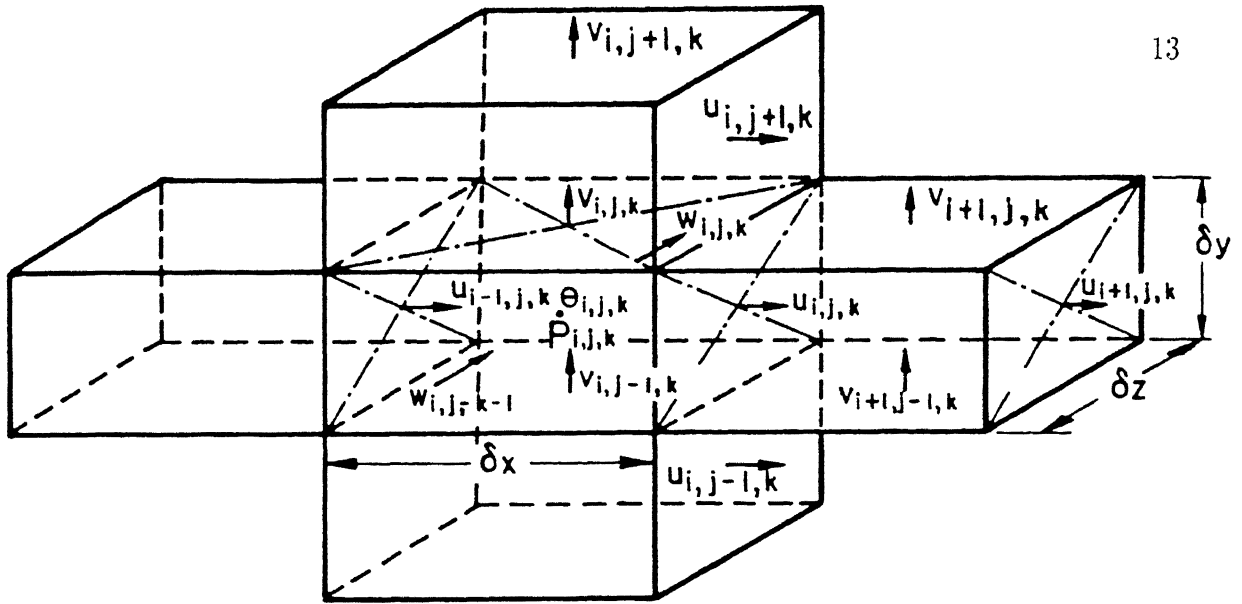


Figure 2.3: Three-dimensional staggered grid showing the locations of the discretized variables

2.6 Numerical Boundary Conditions

We have discussed the boundary conditions of symbolic form. It is necessary to discuss the implementation technique of the boundary condition in the solution code. The boundary conditions are imposed by setting the appropriate velocities in the fictitious (or imaginary) cells surrounding the physical domain.

2.6.1 Boundary Conditions for Confining Walls

The governing differential equations are elliptic in space and parabolic in time. We need the boundary conditions for all the confining surfaces. Since the confining walls at the top and bottom are rigid for the present computation, both the normal and the tangential components of velocity on the wall must be zero. With reference to Fig.2.4, we can write

(for the bottom boundary of the computational domain)

$$\left. \begin{aligned} U_{i,1,k} &= -U_{i,2,k} \\ V_{i,1,k} &= 0 \\ W_{i,1,k} &= -W_{i,2,k} \end{aligned} \right\} \begin{aligned} &\text{for } i = 2 \text{ to } ire \\ &\text{and } k = 2 \text{ to } kre \end{aligned} \quad (2.6)$$

Similarly, for the no-slip right wall, the boundary conditions become

$$\left. \begin{aligned} U_{i,j,1} &= -U_{i,j,2} \\ V_{i,j,1} &= -V_{i,j,2} \\ W_{i,j,1} &= 0 \end{aligned} \right\} \begin{aligned} &\text{for } i = 2 \text{ to } ire \\ &\text{and } j = 2 \text{ to } jre \end{aligned} \quad (2.7)$$

The front plane (inlet plane) is to be provided with the inflow boundary condition. The normal velocity components are set to zero and a uniform or parabolic axial velocity may be deployed. Hence, with reference to Fig.2.4, we can use

$$\left. \begin{aligned} W_{1,j,k} &= -W_{2,j,k} \\ V_{1,j,k} &= -V_{2,j,k} \\ U_{1,j,k} &= 1.0 \end{aligned} \right\} \begin{aligned} &\text{for } j = 2 \text{ to } jre \\ &\text{and } k = 2 \text{ to } kre \end{aligned} \quad (2.8)$$

or, $U_{1,j,k} = 1.5 \left[1 - \left\{ \frac{j_m - j}{j_m} \right\}^2 \right]$

where j_m is the horizontal mid-plane.

Continuative or outflow boundaries always pose a problem for low-speed calculations, because whatever prescription is chosen it can effect the entire flow field upstream. We should follow a prescription that allows fluid to flow out of the computational domain with a minimum of upstream influence. In our present computation, the second derivative of the dependent variables with respect to flow direction are set to zero to ensure smooth transition through the outlet boundary. These can be implemented in the following way:

$$\left. \begin{aligned} U_{i+1,j,k} &= 2U_{i,j,k} - U_{i-1,j,k} \\ V_{i+1,j,k} &= 2V_{i,j,k} - V_{i-1,j,k} \\ W_{i+1,j,k} &= 2W_{i,j,k} - W_{i-1,j,k} \end{aligned} \right\} \begin{aligned} &\text{for } j = 2 \text{ to } jre \\ &\text{and } k = 2 \text{ to } kre \\ &\text{at } i = iim - 2 \end{aligned} \quad (2.9)$$

The governing equations and the boundary conditions discussed so far are described for a three dimensional problem. The two dimensional problem is a subset of the three dimensional problem and the implementation is straightforward.

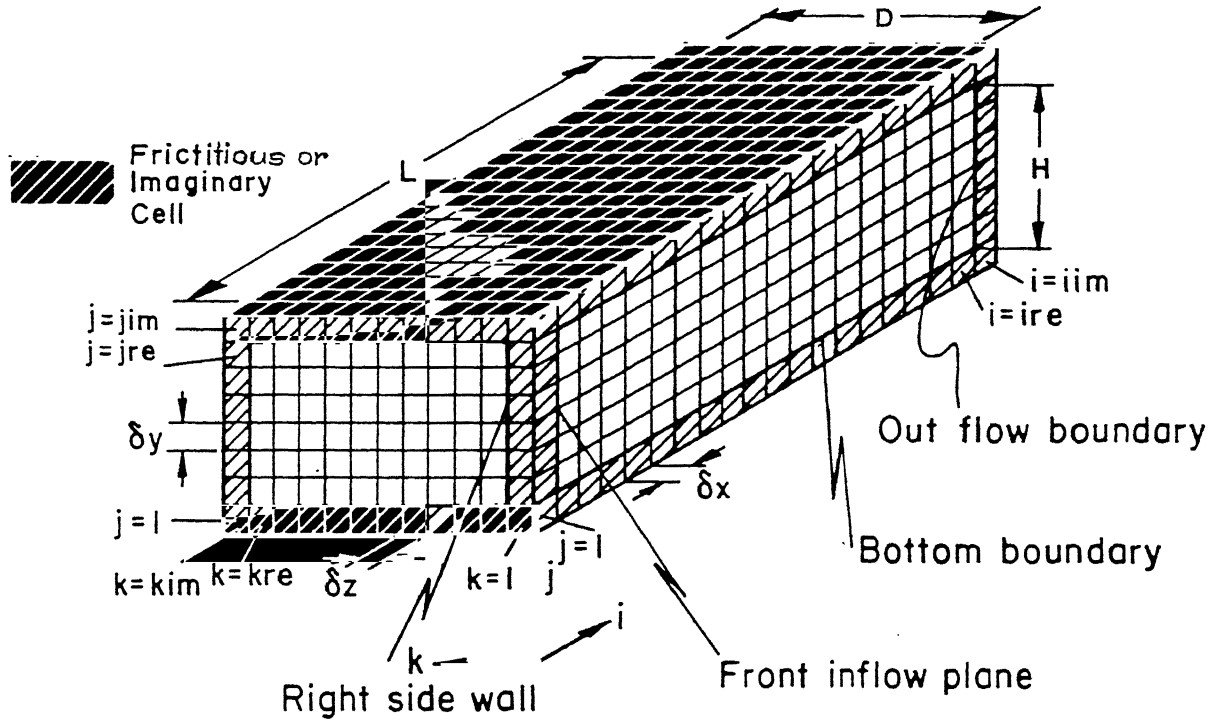


Figure 2.4: Boundary conditions and fictitious boundary cells

2.6.2 Boundary Conditions for the Obstacle

In order to implement the kinematic boundary conditions on the obstacle, the velocity points which are in the domain of the obstacle are set equal to zero. The implementation is explained with the help of a three dimensional flow simulation. Application for a two dimensional case is straight forward. Implementation of the no-slip condition for V- and W-components of velocity along the transverse direction, U-component of velocity along the direction of flow need some manipulations. The boundary conditions are as the following (see Fig.2.5) :

$$U_{i,j,k} = -U_{i,j,k-1} \text{ for } i = ia - 1 \text{ to } ib \text{ at } k = ka \quad (2.10)$$

$$\text{and } U_{i,j,k} = -U_{i,j,k+1} \text{ for } i = ia - 1 \text{ to } ib \text{ at } k = kb \quad (2.11)$$

similarly, for V-component of velocity, we have,

$$V_{i,j,k} = -V_{i,j,k-1} \text{ for } i = ia \text{ to } ib \text{ at } k = ka \quad (2.12)$$

$$V_{i,j,k} = -V_{i,j,k+1} \quad \text{for } i = ia \text{ to } ib \quad \text{at } k = kb \quad (2.13)$$

$$V_{i,j,k} = -V_{i-1,j,k} \quad \text{for } k = ka \text{ to } kb \quad \text{at } i = ia \quad (2.14)$$

$$\text{and } V_{i,j,k} = -V_{i+1,j,k} \quad \text{for } k = ka \text{ to } kb \quad \text{at } i = ib \quad (2.15)$$

finally, for W-component of velocity, one can have

$$W_{i,j,k} = -W_{i-1,j,k} \quad \text{for } k = ka - 1 \text{ to } kb \quad \text{at } i = ia \quad (2.16)$$

$$\text{and } W_{i,j,k} = -W_{i+1,j,k} \quad \text{for } k = ka - 1 \text{ to } kb \quad \text{at } i = ib \quad (2.17)$$

For all the above cases, j varies from 2 to jre

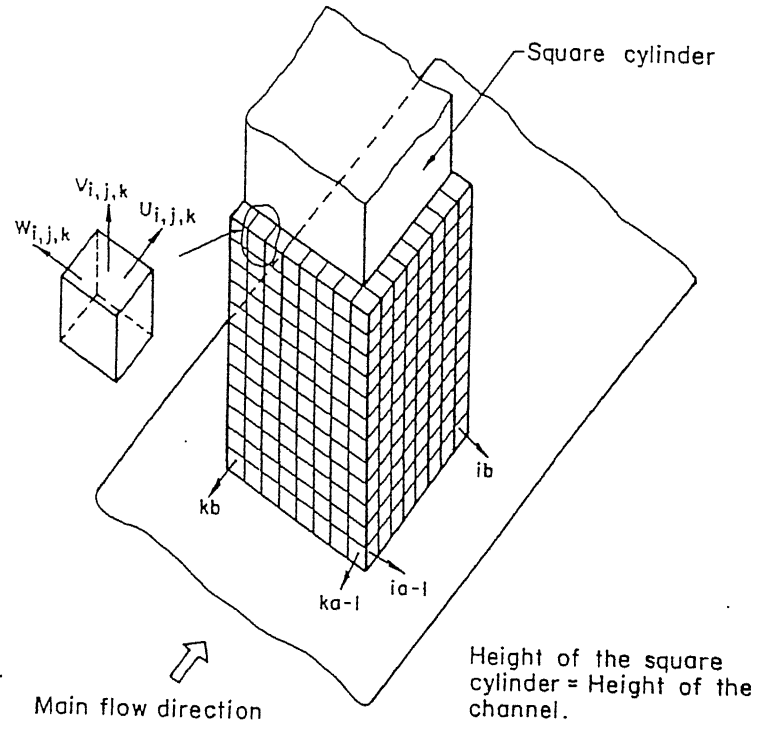


Figure 2.5: Discretization of the three-dimensional square obstacle

2.7 Closure

In the present numerical investigations, the input parameters are Reynolds number, nondimensional length of the channel, inlet velocity profile and the nondimensional ob-

stacle height. For two-dimensional problem, the nondimensional length of the channel is 4.875. The obstacle is placed at a nondimensional distance of 1.375 from inlet. In three-dimensional problem, the nondimensional breadth and height of the channel is 1. The aspect ratio of the obstacle is 1. The nondimensional length of the channel is 3.333. The obstacle is placed at a location whose nondimensional distance from inlet is also 1.

Chapter 3

Solution Procedure

3.1 Solution Algorithm

The nondimensional continuity and momentum equations written in terms of primitive variables in weak conservative forms (equations(2.1) through (2.4)), are solved by using a modified version of Marker And Cell (MAC) algorithm. The original version of the MAC method due to Harlow and Welch (1965) has been modified by Hirt and Cook (1972). In the original MAC method, the pressure field is determined by directly solving Poisson equation for pressure, whereas, in the modified version of MAC algorithm pressure values are calculated by a pressure-velocity iteration procedure. A related technique developed by Chorin (1967) involved a simultaneous iteration on pressure and velocity components. Vieceilli (1971) has shown that the two methods as applied to the MAC algorithm are equivalent.

3.2 Details of the Computational scheme

The MAC is a semi-implicit scheme for solving full Navier-Stokes equations where the advancements of velocity components in the time direction are obtained explicitly by calculating accelerations due to convection, diffusion and pressure gradient. Thus, after obtaining provisional velocity field for a time step, the continuity equation is solved

implicitly to correct the provisional velocity field. Hence MAC is a semi-implicit scheme.

From the guessed velocity and pressure fields, the corrected velocity and pressure fields are obtained by pressure-velocity iteration through the continuity equation. Convergence of this iteration process ensures a divergence-free velocity field for the initial time step. Now, the corrected pressure-velocity fields are used to calculate the velocity field for the next time step by solving the Navier-Stokes equations. The time step $\delta\tau$ for the advancement of the velocities is governed by the stability criteria which are discussed in a subsequent section. However, this explicit time advancement may not lead to a velocity field with zero mass divergence in each cell. The satisfaction of the continuity equation is achieved by adjusting the pressures as well as velocities in each cell through an iterative process, which as mentioned earlier, is equivalent to solution of a Poisson equation for pressure. Details of pressure-velocity iteration procedure is discussed in the following section. The corrected pressure and velocity fields are now used to evaluate the provisional velocities for the next time step and so on. Thus, starting from initial guess fields, the solution advances in time direction until a steady or periodic solution is obtained.

3.3 Discretization of Governing Differential Equation

Because of staggered grid arrangement (Fig.2.3) the velocities are not defined at the nodal points. Whenever required, the velocities at the nodal points are calculated by interpolation of neighbouring velocities. As an example, we can write $U_{i-\frac{1}{2},k} = 0.5(U_{i-1,j,k} + U_{i,j,k})$, but where a product or square of such quality appears, it is customary to interpolate first and then the product to be taken.

For any cell, the discretization of the continuity equation is given by

$$D_{i,j,k} = \frac{U_{i,j,k} - U_{i-1,j,k}}{\delta X} + \frac{V_{i,j,k} - V_{i,j-1,k}}{\delta Y} + \frac{W_{i,j,k} - W_{i,j,k-1}}{\delta Z} \quad (3.1)$$

The discretization of the temporal derivatives in equations (2.1) to (2.4) is done by

a forward differencing

$$\frac{\partial U}{\partial \tau} = \frac{U_{i,j,k}^{n+1} - U_{i,j,k}^n}{\delta \tau} \quad (3.2)$$

The convective terms of the momentum equations are discretized by a weighted average scheme which combines the upwind and central differencing to achieve the stability of upwind and formal accuracy of the central differencing (Hirt, Nichols and Romero, 1975). The discretization of one of the convective terms is shown below:

$$\begin{aligned} \frac{\partial(UV)}{\partial Y} = & \frac{1}{4\delta Y} [(V_{i,j,k} + V_{i+1,j,k})(U_{i,j,k} + U_{i,j+1,k}) \\ & + \alpha_p |(V_{i,j,k} + V_{i+1,j,k})| (U_{i,j,k} - U_{i,j+1,k}) \\ & - (V_{i,j-1,k} + V_{i+1,j-1,k})(U_{i,j-1,k} + U_{i,j,k}) \\ & - \alpha_p |(V_{i,j-1,k} + V_{i+1,j-1,k})| (U_{i,j-1,k} - U_{i,j,k})] \end{aligned} \quad (3.3)$$

The factor α_p determines the relative weightage of the central and upwind differencing. $\alpha_p = 0$ gives simple a central differencing and $\alpha_p = 1$ leads to a second upwind differencing. The value of this factor is between 0.2 and 0.3.

3.4 Pressure-Velocity Iteration

In the original MAC method the Poisson equation was solved for pressure. The modification due to Hirt and Cook (1972) enables one to solve the Poisson equation for pressure in such a way that the velocity and pressure fields are corrected in an iterative procedure.

The velocities are advanced explicitly for the next time step from the momentum equations if the velocities and pressures are known at any time step. But these velocities do not necessarily describe a meaningful solution if there is a non-zero divergence in any cell. The pressures distribution are correct if it is accompanied by a zero divergence in each cell. The pressures have to be corrected so that there is no accumulation or annihilation of mass anywhere in the domain. Corrections to pressures are applied in an iterative manner as described by Hirt and Cook (1972).

The method of pressure-velocity iteration is as follows. The relationship between

the explicitly advanced velocity components at $(n + 1)$ th time level and those at the previous n th time level can be written as

$$\tilde{U}_{i,j,k}^{n+1} = U_{i,j,k}^n + \left(\frac{\delta\tau}{\delta X} \right) (P_{i,j,k}^n - P_{i+1,j,k}^n) + \delta\tau [RESIDU]_{i,j,k}^n \quad (3.4)$$

where $[RESIDU]_{i,j,k}^n$ is the discretized form of

$$\left[-\frac{\partial U^2}{\partial X} - \frac{\partial UV}{\partial Y} - \frac{\partial UW}{\partial Z} + \frac{\nabla^2 U}{Re} \right] \quad (3.5)$$

at the (i, j, k) cell evaluated with the velocity values at the n th time step.

On the other hand, the corrected velocity components, which are still unknown, are related to the correct pressure (unknown) in the manner

$$U_{i,j,k}^{n+1} = U_{i,j,k}^n + \left(\frac{\delta\tau}{\delta X} \right) (P_{i,j,k}^{n+1} - P_{i+1,j,k}^{n+1}) + \delta\tau [RESIDU]_{i,j,k}^n \quad (3.6)$$

from equations (3.4) and (3.6) one can write

$$U_{i,j,k}^{n+1} - \tilde{U}_{i,j,k}^{n+1} = \left(\frac{\delta\tau}{\delta X} \right) (P'_{i,j,k} - P'_{i+1,j,k}) \quad (3.7)$$

where $P'_{i,j,k} = P_{i,j,k}^{n+1} - P_{i,j,k}^n$

Neither $P'_{i,j,k}$ nor $U_{i,j,k}^{n+1}$ are explicitly known at this stage so that one can be calculated with the help of the other. Calculations are done in an iterative cycle and we can write

$$U_{i,j,k}^{n+1} \longrightarrow \tilde{U}_{i,j,k}^{n+1} + \left(\frac{\delta\tau}{\delta X} \right) (P'_{i,j,k} - P'_{i+1,j,k}) \quad (3.8)$$

In the similar manner the other velocities can be written as

$$\text{Corrected} \quad \quad \text{Estimated} \quad \quad \text{Correction} \quad (3.9)$$

$$U_{i-1,j,k}^{n+1} \longrightarrow \tilde{U}_{i-1,j,k}^{n+1} - \left(\frac{\delta\tau}{\delta X} \right) (P'_{i,j,k} - P'_{i-1,j,k}) \quad (3.10)$$

$$V_{i,j,k}^{n+1} \longrightarrow \tilde{V}_{i,j,k}^{n+1} + \left(\frac{\delta\tau}{\delta Y} \right) (P'_{i,j,k} - P'_{i,j+1,k}) \quad (3.11)$$

$$V_{i,j-1,k}^{n+1} \longrightarrow \tilde{V}_{i,j-1,k}^{n+1} - \left(\frac{\delta\tau}{\delta Y} \right) (P'_{i,j,k} - P'_{i,j-1,k}) \quad (3.12)$$

$$W_{i,j,k}^{n+1} \longrightarrow \tilde{W}_{i,j,k}^{n+1} + \left(\frac{\delta\tau}{\delta Z} \right) (P'_{i,j,k} - P'_{i,j,k+1}) \quad (3.13)$$

$$W_{i,j,k-1}^{n+1} \longrightarrow \tilde{W}_{i,j,k-1}^{n+1} - \left(\frac{\delta\tau}{\delta Z} \right) (P'_{i,j,k} - P'_{i,j,k-1}) \quad (3.14)$$

The correction is done through continuity equation. Plugging in the relationship into the continuity equation we get

$$\begin{aligned} & \left[\frac{U_{i,j,k}^{n+1} - U_{i-1,j,k}^{n+1}}{\delta X} + \frac{V_{i,j,k}^{n+1} - V_{i,j-1,k}^{n+1}}{\delta Y} + \frac{W_{i,j,k}^{n+1} - W_{i,j,k-1}^{n+1}}{\delta Z} \right] \\ = & \left[\frac{\tilde{U}_{i,j,k}^{n+1} - \tilde{U}_{i-1,j,k}^{n+1}}{\delta X} + \frac{\tilde{V}_{i,j,k}^{n+1} - \tilde{V}_{i,j-1,k}^{n+1}}{\delta Y} + \frac{\tilde{W}_{i,j,k}^{n+1} - \tilde{W}_{i,j,k-1}^{n+1}}{\delta Z} \right] \\ - & \delta\tau \left[\frac{P'_{i+1,j,k} - 2P'_{i,j,k} + P'_{i-1,j,k}}{\delta X^2} \right] \\ - & \delta\tau \left[\frac{P'_{i,j+1,k} - 2P'_{i,j,k} + P'_{i,j-1,k}}{\delta Y^2} \right] \\ - & \delta\tau \left[\frac{P'_{i,j,k+1} - 2P'_{i,j,k} + P'_{i,j,k-1}}{\delta Z^2} \right] \end{aligned} \quad (3.15)$$

At this stage, the pressure corrections in the neighbouring cells are neglected. Therefore, we get the velocity corrections in the form,

$$U_{i,j,k}^{n+1} \longrightarrow \tilde{U}_{i,j,k}^{n+1} + \left(\frac{\delta\tau}{\delta X} \right) (P'_{i,j,k}) \quad (3.16)$$

$$U_{i-1,j,k}^{n+1} \longrightarrow \tilde{U}_{i-1,j,k}^{n+1} - \left(\frac{\delta\tau}{\delta X} \right) (P'_{i,j,k}) \quad (3.17)$$

$$V_{i,j,k}^{n+1} \longrightarrow \tilde{V}_{i,j,k}^{n+1} + \left(\frac{\delta\tau}{\delta Y} \right) (P'_{i,j,k}) \quad (3.18)$$

$$V_{i,j-1,k}^{n+1} \longrightarrow \tilde{V}_{i,j-1,k}^{n+1} - \left(\frac{\delta\tau}{\delta Y} \right) (P'_{i,j,k}) \quad (3.19)$$

$$W_{i,j,k}^{n+1} \longrightarrow \tilde{W}_{i,j,k}^{n+1} + \left(\frac{\delta\tau}{\delta Z} \right) (P'_{i,j,k}) \quad (3.20)$$

$$W_{i,j,k-1}^{n+1} \longrightarrow \tilde{W}_{i,j,k-1}^{n+1} - \left(\frac{\delta\tau}{\delta Z} \right) (P'_{i,j,k}) \quad (3.21)$$

The continuity equation takes the following form after neglecting the pressures corrections in the neighbouring cells,

$$\begin{aligned} & \left[\frac{U_{i,j,k}^{n+1} - U_{i-1,j,k}^{n+1}}{\delta X} + \frac{V_{i,j,k}^{n+1} - V_{i,j-1,k}^{n+1}}{\delta Y} + \frac{W_{i,j,k}^{n+1} - W_{i,j,k-1}^{n+1}}{\delta Z} \right] \\ &= \left[\frac{\tilde{U}_{i,j,k}^{n+1} - \tilde{U}_{i-1,j,k}^{n+1}}{\delta X} + \frac{\tilde{V}_{i,j,k}^{n+1} - \tilde{V}_{i,j-1,k}^{n+1}}{\delta Y} + \frac{\tilde{W}_{i,j,k}^{n+1} - \tilde{W}_{i,j,k-1}^{n+1}}{\delta Z} \right] \\ &+ 2 \left(\frac{\delta \tau}{\delta X^2} \right) (P'_{i,j,k}) + 2 \left(\frac{\delta \tau}{\delta Y^2} \right) (P'_{i,j,k}) + 2 \left(\frac{\delta \tau}{\delta Z^2} \right) (P'_{i,j,k}) \end{aligned} \quad (3.22)$$

or,

$$0 = D_{i,j,k} + P'_{i,j,k} \left[2\delta\tau \left\{ \frac{1}{\delta X^2} + \frac{1}{\delta Y^2} + \frac{1}{\delta Z^2} \right\} \right] \quad (3.23)$$

or,

$$P'_{i,j,k} = -\omega_0(D_{i,j,k}) / \left[2\delta\tau \left\{ \frac{1}{\delta X^2} + \frac{1}{\delta Y^2} + \frac{1}{\delta Z^2} \right\} \right] \quad (3.24)$$

where ω_0 is an over relaxation factor which is introduced to accelerate the pressure correction process. Usually a value of 1.7 is used. After calculating $P'_{i,j,k}$, velocities in each cell are corrected according to the equations (3.16) to (3.21) and the pressure in each cell is adjusted as

$$P_{i,j,k}^{n+1} \longrightarrow P_{i,j,k}^n + P'_{i,j,k} \quad (3.25)$$

This process is continued until the velocity divergence in each cell vanishes. If the velocity boundary conditions are correct and a divergence-free converged velocity field is obtained, eventually correct pressures will be evolved in all the cells including the cells on the boundary. This feature of modified MAC method has been discussed in more details by Peyret and Taylor (1983). However, it was also shown by Brandt, Dendy and Ruppel that the aforesaid pressure-velocity iteration procedure is equivalent to solution of Poisson Equation for pressure.

3.5 Stability Criteria

For a given mesh the choice of the time step is determined through stability analysis which has to take care of two conditions. First, fluid should not allowed to cross more than

one cell in one time step . This restriction is derived from the Courant-Friedrichs-Lewy (CFL) condition given by

$$\delta\tau_1 < \min \left\{ \frac{\delta X}{|U|}, \frac{\delta Y}{|V|}, \frac{\delta Z}{|W|} \right\} \quad (3.26)$$

where the minimum is with respect to every cell in the domain. Typically $\delta\tau$ is chosen equal to one-third to two-third of the minimum cell transient time.

Secondly, when a nonzero value of kinematic viscosity is used, momentum must not diffuse more than approximately one cell in one time step. A linear stability analysis shows that the restrictions on grid Fourier number will yield

$$\delta\tau_2 < \frac{1}{2} \frac{(\delta X^2)(\delta Y^2)(\delta Z^2)}{(\delta X^2) + (\delta Y^2) + (\delta Z^2)} Re \quad (3.27)$$

Finally, the minimum of the above two time-steps is chosen for the computation.

The term α_p in the discretization of the convective terms of the Navier-Stokes equations gives the desired amount of upstream (donor cell) differencing. When $\alpha_p = 0$, a space-centred differencing is obtained and $\alpha_p = 1$ leads to full upstream or donor cell form. In general, α_p should be chosen slightly larger than the maximum value of

$$\left| \frac{U\delta\tau}{\delta X} \right| \quad \text{or} \quad \left| \frac{V\delta\tau}{\delta Y} \right| \quad \text{or} \quad \left| \frac{W\delta\tau}{\delta Z} \right| \quad (3.28)$$

occurring in the entire domain. In other words,

$$1 > \alpha_p > \max \left\{ \left| \frac{U\delta\tau}{\delta X} \right|, \left| \frac{V\delta\tau}{\delta Y} \right|, \left| \frac{W\delta\tau}{\delta Z} \right| \right\} \quad (3.29)$$

Doc. No. A.118019

Chapter 4

Multigrid Implementation

4.1 Objective

It has been experienced that most of the computational work of the MAC algorithm is due to the pressure-velocity iteration. The purpose of our investigation is to reduce computational work by the application of a multigrid techniques to the pressure-velocity iteration. In order to explain the computational strategy of the multigrid technique, we shall start with the basic discretized equations which have been explained in Chapter-3. However, we shall use the symbolic forms which are more convenient for explaining of multigrid strategy. The difference equations approximating the momentum equations are:

$$\left. \begin{aligned} U_{i,j,k}^{n+1} - U_{i,j,k}^n + (\delta\tau/\delta X)(P_{i+1,j,k}^{n+1} - P_{i,j,k}^{n+1}) &= a_{i,j,k}^n \\ V_{i,j,k}^{n+1} - V_{i,j,k}^n + (\delta\tau/\delta Y)(P_{i,j+1,k}^{n+1} - P_{i,j,k}^{n+1}) &= b_{i,j,k}^n \\ W_{i,j,k}^{n+1} - W_{i,j,k}^n + (\delta\tau/\delta Z)(P_{i,j,k+1}^{n+1} - P_{i,j,k}^{n+1}) &= c_{i,j,k}^n \end{aligned} \right\} \quad (4.1)$$

where the superscripts n stands for the time step ; a, b, c represent the combined convective-diffusive terms. The continuity equation is discretised as follows:

$$D_{i,j,k}^{n+1} \equiv \frac{(U_{i,j,k}^{n+1} - U_{i-1,j,k}^{n+1})}{\delta X} + \frac{(V_{i,j,k}^{n+1} - V_{i,j-1,k}^{n+1})}{\delta Y} + \frac{(W_{i,j,k}^{n+1} - W_{i,j,k-1}^{n+1})}{\delta Z} = 0 \quad (4.2)$$

The computational sequences of equations (4.1) and (4.2) is shown in Fig.4.1.

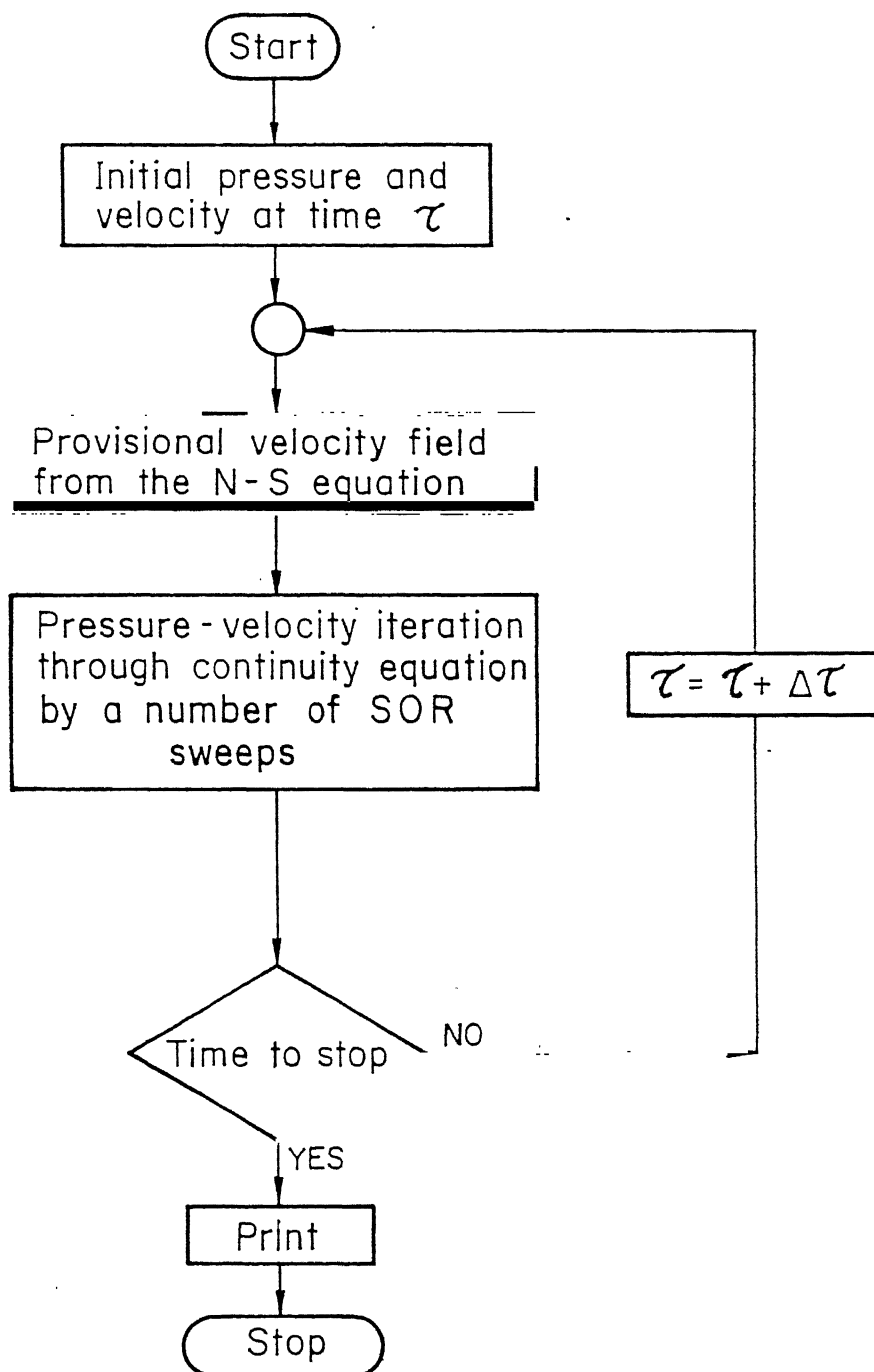


Figure 4.1: Computational sequence of the MAC algorithm

The treatment of the continuity equation together with the pressure-velocity iteration in MAC method is equivalent to a solution of Poisson-equation for pressure which is given by

$$P'(\bar{X}) = \frac{-\omega_0 D(\bar{X})}{\left[2\delta\tau \left\{ \frac{1}{\delta X^2} + \frac{1}{\delta Y^2} + \frac{1}{\delta Z^2} \right\} \right]} \quad (4.3)$$

The Gauss-Seidel sweep is performed to reduce D in each cell of the computational grid.

During the initial stage of computations, a large number of relaxation sweeps for each time step is necessary in order to reduce the divergence (error) for some initial value D_I below a given upper bound $D_F(\sim 10^{-4})$.

These errors reduced by such relaxation methods may roughly be divided into low and high frequency components corresponding to meshsize h . The convergence usually slows down after the high frequency components being smoothened out. Convergence properties for the reduction of a low frequency error component corresponding to h can be improved by treating this component on a coarser grid with meshsize $2h$ where it appears as high frequency component corresponding to $2h$.

4.2 Grid Arrangement

The multigrid technique uses several grid levels in cyclic order to accelerate the convergence of the solution. But the generation of grids needs special care such that it does not affect the boundary conditions. Generally, the calculation is started with the coarsest grid. Then this coarsest grid is splitted into several levels by doubling the number of grids (or halving the mesh size). The finest grid is used for solving the basic difference equations. Calculation can also be started from the finest grid depending on the type of cycling scheme and equations to be solved. A typical two-dimensional grid arrangement is shown in Fig.4.2 for three different grid levels. An extension to three dimensional geometry is straight-forward.

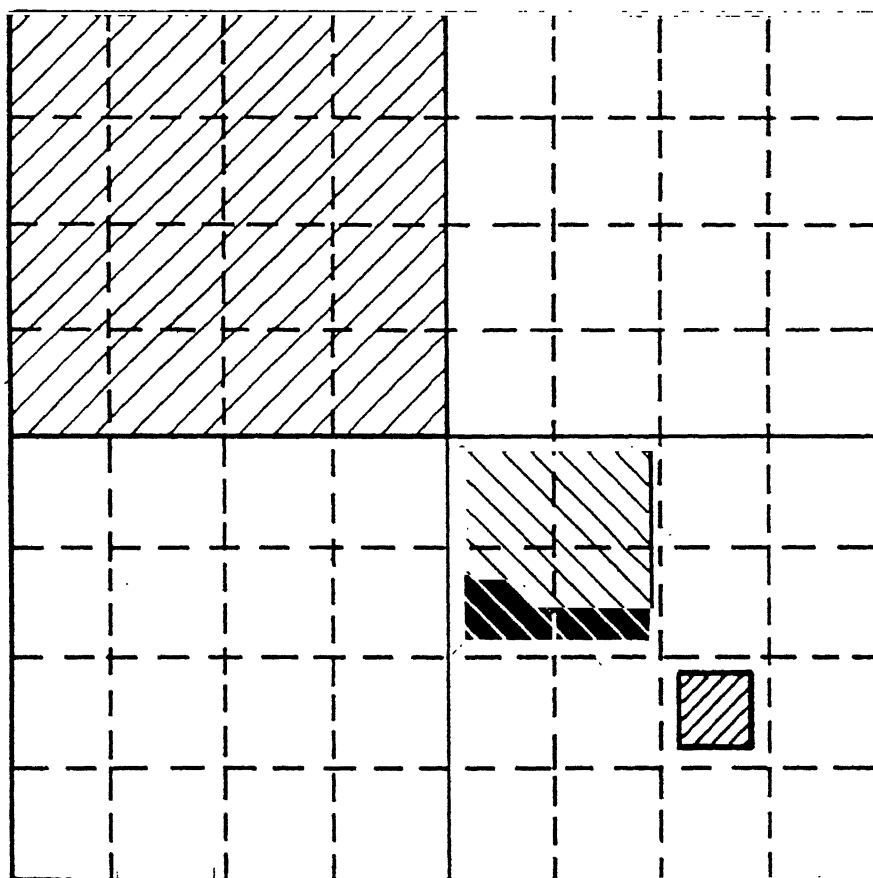


Figure 4.2: Three different grid levels for a multigrid technique

4.3 Multigrid Strategy

In multigrid method error components of different frequencies are reduced on a number of grids having successive coarseness, Brandt *et al* (1980) suggested the multigrid technique of equation (4.2) can be carried out by correction scheme (CS) mode because of the linear character of the differential operator of the continuity equation.

Several cycling schemes for fine to coarse grids are possible. In one strategy V-cycles are used (Fig.4.3) to compute equation (4.3) on a fine grid and a number of correction equations (4.5) and (4.6) on successive coarser grids.

A V-cycle starts from the fine grid and performs a previously specified number of iterations on the fine grid and subsequent coarse grids. RESTRICTION is the process of obtaining a coarse grid solution from a finer grid. A V-cycle ends at the finest grid by performing iteration after corrections are prolonged on each grid level. PROLONGATION refers to extrapolation of coarse grid values to finer grids. The symbols which we shall follow in the subsequent sections are as follows:

$$\begin{aligned} P &\equiv \text{Nondimensional pressure field} \\ U_l &\equiv (U, V, W) \equiv \text{Velocity field} \\ h(\delta X, \delta Y, \delta Z) &\equiv \text{Mesh size} \\ \text{and } \overline{X} &\equiv \text{Cell center} \end{aligned}$$

4.3.1 Restriction

To start with the Gauss-Seidel relaxation sweeps are done with the correction equation (4.3) on finest grid. At this stage we can write

$$D_l = \text{div } U_l \quad \text{on finest grid } (l = m) \quad (4.4)$$

where, *div* is a divergence operator

Subsequently the Gauss-Seidel relaxation sweeps are accomplished on the coarser grids ($l < m$). The operation can be stated as

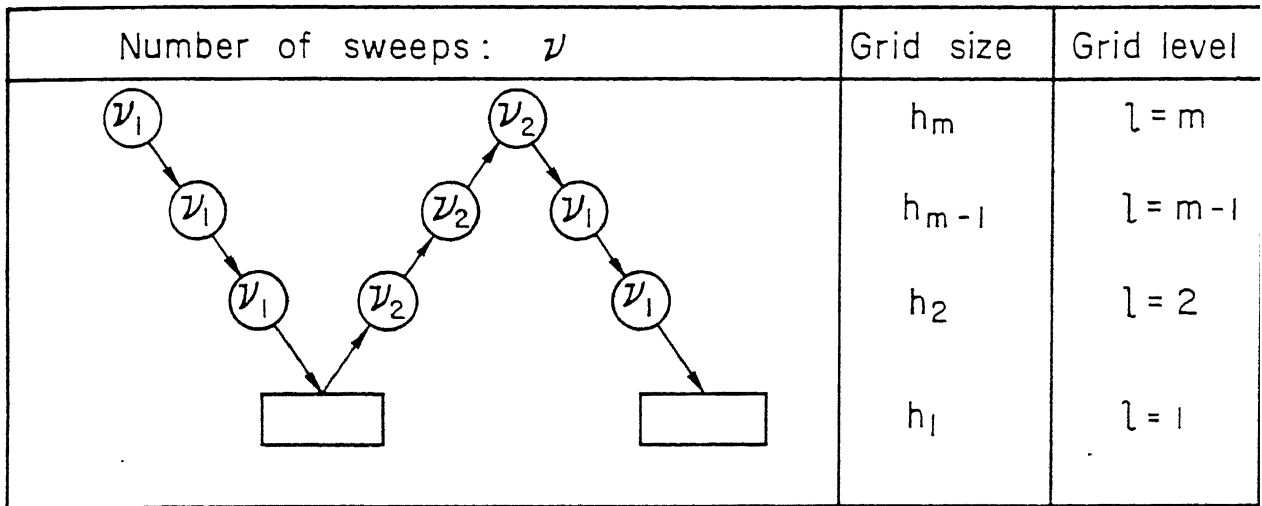


Figure 4.3: A V - cycle (CS mode)

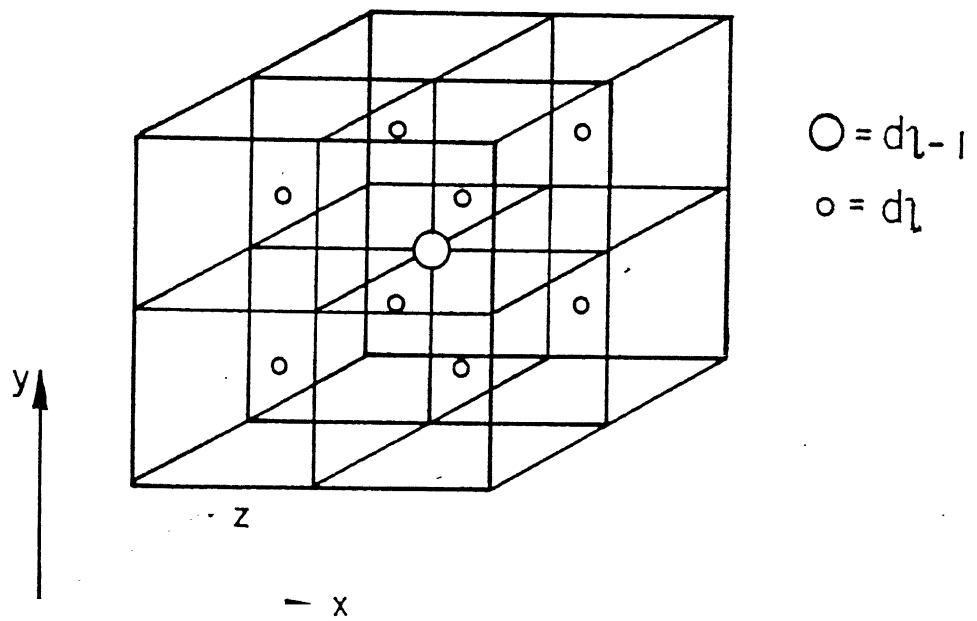


Figure 4.4: Restriction of residuals (defects) to coarse grid

$$D_l = \text{div } U_l + \bar{d}_l \quad \text{starting with } U_l = 0 ; P_l = 0 \quad (4.5)$$

where, \bar{d}_l = sum of restricted defects (divergence) of grids from l to $(l-1)$, l being $\leq m$.

After a specified number of iterations at a particular grid level, next coarser grid will be taken up and the divergence (defect) is restricted for the next grid. The general algorithm is:

$$\text{Computation of defect : } d_l = \sum_l^m D_l \quad (4.6)$$

$$\text{Restriction of defect(divergence) : } \bar{d}_l = I_l^{l-1} d_l \quad (4.7)$$

where, I_l^{l-1} is restriction operator which is explained in Fig.4.4. Numerically the operator can be expressed as

$$\bar{d}_{l-1} = I_l^{l-1} d_l \equiv \frac{1}{n} \sum_n d_l \quad (4.8)$$

The process of taking up next level of coarser grid continues till the coarsest grid is reached. RELAXATION *until convergence is carried out only on the coarsest grid ($l=1$), where the calculation is cheap because of the number of grid points*. Experience shows that a number of sweeps ($\nu_1 \leq 3$) are sufficient at each grid level. However, such specified number of sweeps at each grid level may require multiple V-cycles. A typical value of number of V-cycles has been reported as 8 (see Brockmeir *et al*, 1986). In order to reduce the number of cycles, an adaptive cycling scheme is suggested (Vanka, 1986b). In adaptive cycling scheme, a fixed error reduction is desired rather than a fixed number of iterations.

Let e^k be the error on grid l at k th iteration, then switching over to $(l-1)$ grid is recommended if $(e^{k-1}/e^k) = \delta_v$ is achieved. We have used the adaptive cycling scheme and the value of δ_v has been chosen as 0.6. Iterations are performed on grid l until the above criterion is met.

For two dimensional problem the restriction can be explained with the help of Fig.4.5. Let (ic, jc) and (if, jf) are the coarse and fine grid indices respectively. One can write

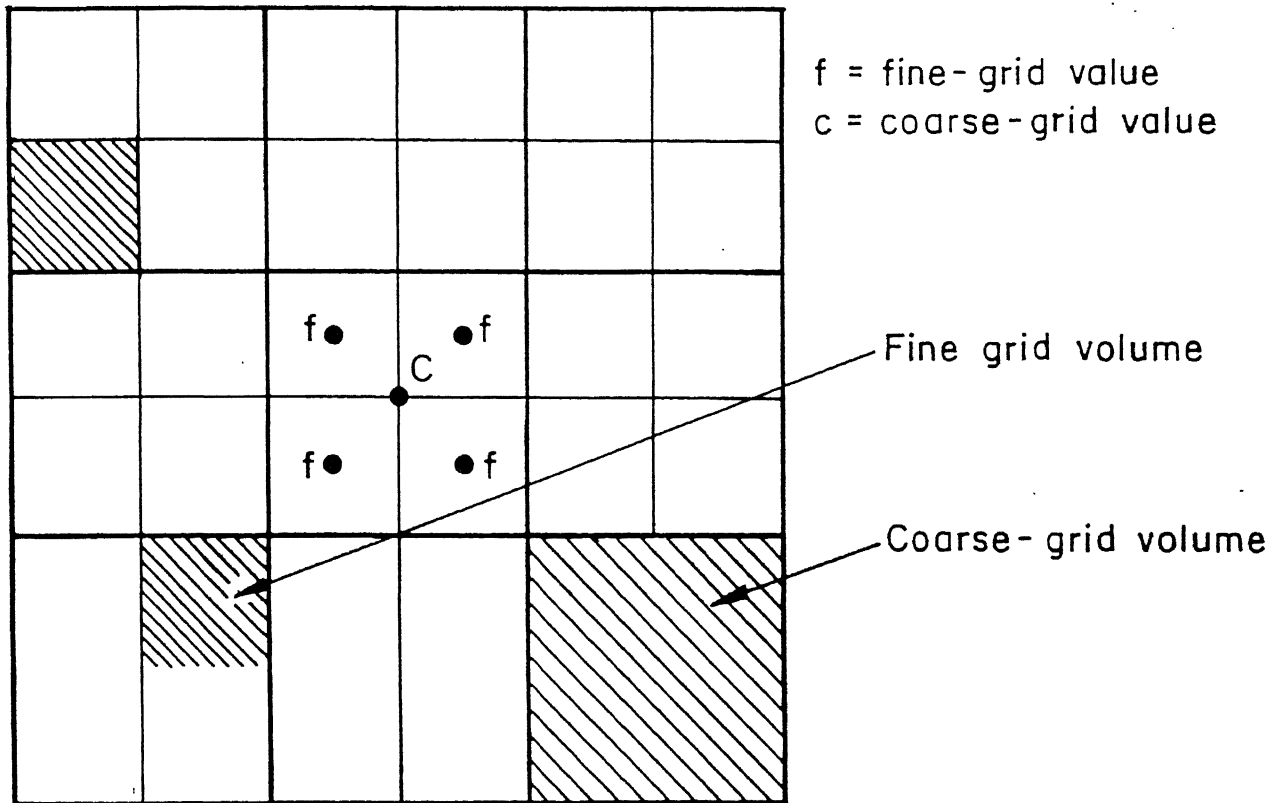


Figure 4.5: Fine- and coarse-grid values of restriction

$$if = 2 \times ic - 1$$

$$\text{and } jf = 2 \times jc - 1$$

The restriction operator explained by equation(4.8) can be written as

$$d^c(ic, jc) = 0.25 \times [d^f(if, jf) + d^f(if, jf - 1) + d^f(if - 1, jf) + d^f(if - 1, jf - 1)] \quad (4.9)$$

However, while switching over to the next coarser grid, the velocities and pressure at each grid level are stored in a separate array.

4.3.2 Prolongation

As it has been stated earlier, after having achieved convergence in coarsest grid, the values of pressures are prolonged to the next finer grid. Weighted interpolation is used to obtain finer grid pressures corrections out of coarse grid pressures (Hackbuch and Trottenberg, 1982). For simplicity this interpolation is shown schematically for a two dimensional geometry in Fig.4.6. Most commonly used interpolation is trilinear. A trilinear technique considers a linear variation in each spatial direction. For a uniform two dimensional grid, one can write

$$\left. \begin{aligned} f_1 &= (1/16)(9D + 3C + 3A + B) \\ f_2 &= (1/16)(9C + 3B + 3D + A) \\ f_3 &= (1/16)(9A + 3B + 3D + C) \\ f_4 &= (1/16)(9B + 3A + 3C + D) \end{aligned} \right\} \quad (4.10)$$

In terms of operators, as it was done in case of restriction, the equations (4.10) can be expressed as

$$\Delta P'_{f3,l} = I_{l-1}^l(P'_{nb,l-1}) = \frac{1}{16}(9P'_A + 3P'_B + 3P'_D + P'_C)_{l-1} \quad (4.11)$$

The corrections of the finer grid pressure and velocity approximations are then carried out in the following way

$$\left. \begin{aligned} \Delta P'_l(\bar{X}) &= I_{l-1}^l(P'_{nb,l-1}) \\ P'_l(\bar{X}) &\leftarrow P'_l(\bar{X}) + \Delta P'_l(\bar{X}) \\ U_l(\bar{X} + h/2) &\leftarrow U_l(\bar{X} + h/2) + (\Delta\tau/h) [\Delta P'_l(\bar{X}) - \Delta P'_l(\bar{X} + h)] \end{aligned} \right\} \quad (4.12)$$

After prolongation, only one sweep ($\nu_2 = 1$) is good enough for each grid level.

In three dimensional problems during calculation from coarser to finer grid, the value at each node will involve eight neighbouring values. This tantamounts to

$$\begin{bmatrix} \Delta P'_{i,j,k} \\ \Delta P'_{i+1,j,k} \\ \Delta P'_{i,j+1,k} \\ \Delta P'_{i,j,k+1} \\ \Delta P'_{i,j+1,k+1} \\ \Delta P'_{i+1,j,k+1} \\ \Delta P'_{i+1,j+1,k} \\ \Delta P'_{i+1,j+1,k+1} \end{bmatrix}_l = I_{l-1}^l \begin{bmatrix} P'_{i,j,k} \\ P'_{i+1,j,k} \\ P'_{i,j+1,k} \\ P'_{i,j,k+1} \\ P'_{i,j+1,k+1} \\ P'_{i+1,j,k+1} \\ P'_{i+1,j+1,k} \\ P'_{i+1,j+1,k+1} \end{bmatrix}_{l-1} \quad (4.13)$$

where

$$I_{l-1}^l = \frac{1}{64} \begin{bmatrix} 27 & 9 & 9 & 9 & 3 & 3 & 3 & 1 \\ 9 & 27 & 3 & 3 & 1 & 9 & 9 & 3 \\ 9 & 3 & 27 & 3 & 9 & 1 & 9 & 3 \\ 9 & 3 & 3 & 27 & 9 & 9 & 1 & 3 \\ 3 & 1 & 9 & 9 & 27 & 3 & 3 & 9 \\ 3 & 9 & 1 & 9 & 3 & 27 & 3 & 9 \\ 3 & 9 & 9 & 1 & 3 & 3 & 27 & 9 \\ 1 & 3 & 3 & 3 & 9 & 9 & 9 & 27 \end{bmatrix}$$

As it can be seen from Fig.4.6, pressure corrections in the cells on the boundary can not be calculated out of coarse grid pressure corrections (P'_{l-1}). The pressure corrections at the boundary cells are obtained from the inner pressure correction terms ($\Delta P'_l$ s) by linear extrapolation normal to the boundary.

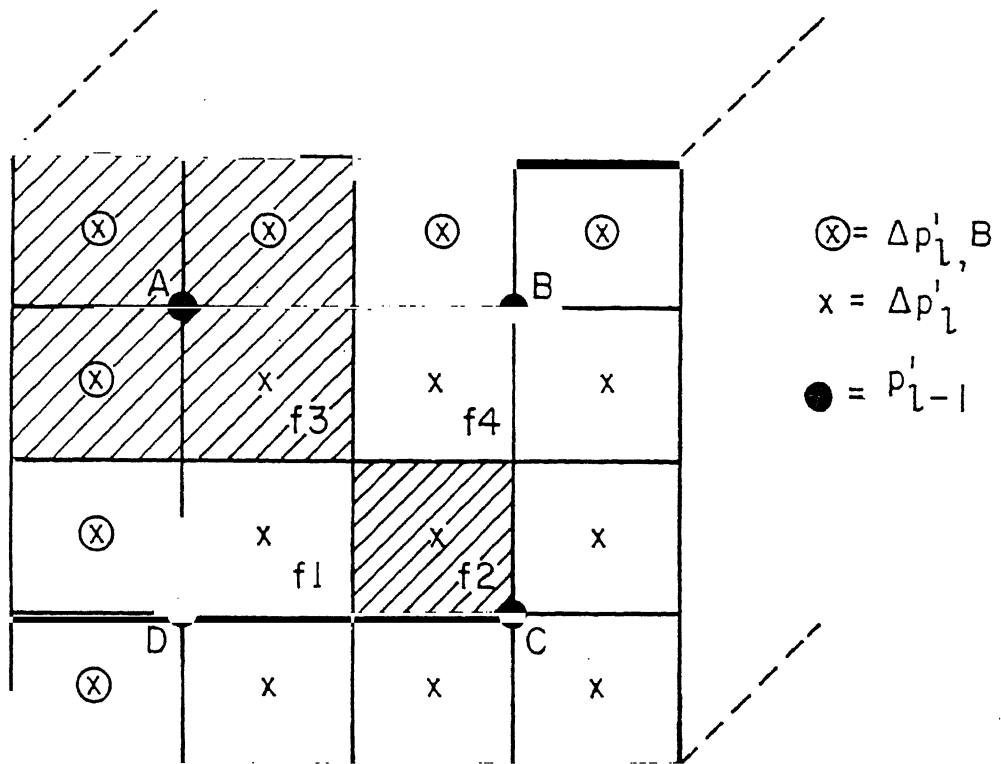


Figure 4.6: Interpolation of coarse grid pressure corrections to finer grid

4.3.3 Velocity Boundary Conditions for Multigrid

It has already been discussed that the velocity boundary conditions are needed to solve equation(4.3). The boundary conditions for pressure are not needed.

$$U_{l,B} = \left. \begin{array}{l} G \text{ for } l = m \\ 0 \text{ for } l < m \end{array} \right\} \quad (4.14)$$

$$\text{and } G = \left. \begin{array}{l} g_u(x, y, z) \\ g_v(x, y, z) \\ g_w(x, y, z) \end{array} \right\} \quad (4.15)$$

where g_u , g_v and g_w are the boundary conditions for the integration domain and the subscript B stands for the boundary.

4.4 Closure

The important aspects of a multigrid computer program are the RESTRICTION, RELAXATION and PROLONGATION. These must be carefully coded and checked out. The total storage necessary (excluding boundaries) is the sum for all grids. For a two dimensional domain, this is

$$\begin{aligned} & m \times n + \frac{m}{2} \times \frac{n}{2} + \frac{m}{4} \times \frac{n}{4} + \cdots \\ & = m \times n \left(1 + \frac{1}{4} + \frac{1}{16} + \cdots \right) = \frac{4m}{3} \times n \end{aligned}$$

where $m \times n$ is the storage on the finest grid. Extension for a three dimensional domain is straight forward.

Chapter 5

Results and Discussions

5.1 Flow Simulation

The numerical investigations of the structure of confined wakes behind a square cylinder for two-dimensional and three-dimensional cases are presented. The numerical flow visualization provides the details of the vortex-shedding phenomenon.

Experimental and numerical studies have shown that the vortex shedding behind the cylinder introduces periodicity at moderate Reynolds numbers in the flow field. The nondimensional Strouhal number which varies with Reynolds number as well as with the blockage ratio characterizes the unsteady periodicity of the wake. The damping of the periodicity in the downstream of the flow may be attributed to the influence of sidewalls on the flow structure. The present study has analyzed the fundamental flow structure and the nondimensional relationships characterizing the vortex-shedding frequency.

5.1.1 Two-Dimensional Flow in a Channel With a Built-in Square Cylinder

For the computation of the present problem, MAC algorithm with 314×66 grid has been used. Uniform grids are deployed throughout the calculation domain. Computations have been carried out in a channel of length $L/H = 4.875$. The geometrical centre of the

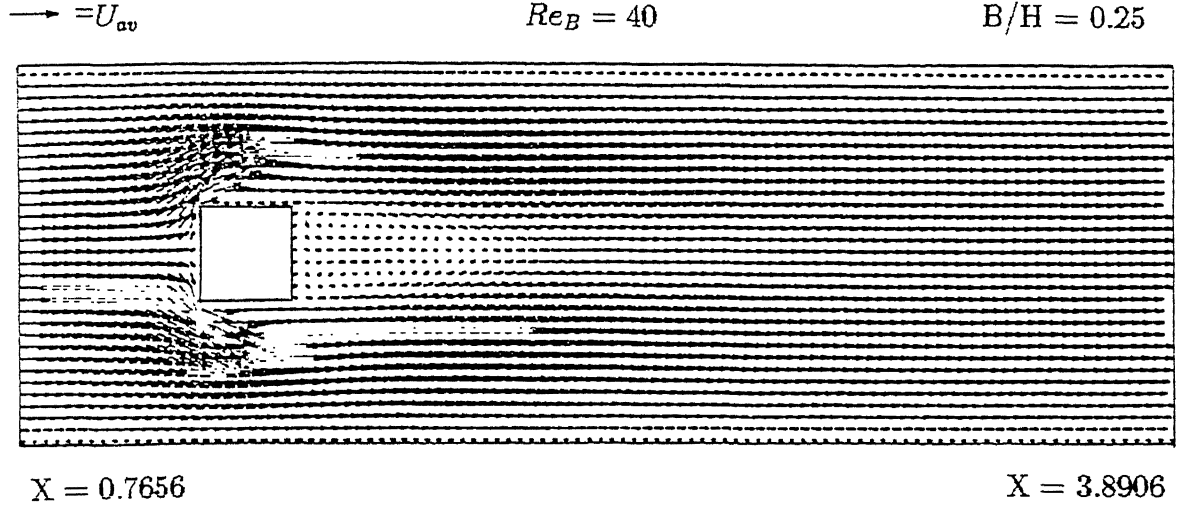


Figure 5.1: Attached vortices behind the obstacle at $Re_B = 40$

square cylinder is located at a distance $X_R = 1.375$ from the inlet. The channel and the cylinder axes are aligned (Fig.2.1(a)). The aspect ratio of the square cylinder is one. The simulation is carried out with two different blockage ratios (B/H), namely, 0.125 and 0.25. The Reynolds number based on the cylinder height, Re_B is used as the input parameter.

The structure of the wake and its functional relationship with Reynolds number are studied by varying the Reynolds number for the same blockage and aspect ratios. In Fig.5.1, a steady solution for $B/H = 0.25$ and Reynolds number $Re_B = 40$ is shown. The recirculating wake is extended to nearly twice the obstacle width in the downstream of the obstacle. Figure 5.2 also shows a symmetric wake for a Reynolds number of 60. Comparison of the Figures 5.1 and 5.2 shows that the extent of the recirculating wake increases with the increase in Reynolds number. The flow field is steady in both the cases. The flow with Reynolds number of 60 does not indicate any vortex shedding. But at $Re_B = 80$, the wake loses its original symmetry and the flow becomes periodic in the near wake (Fig.5.3(a)). However, the periodicity is suppressed in the downstream of the square cylinder by the channel walls and the velocity profile at the exit of the channel

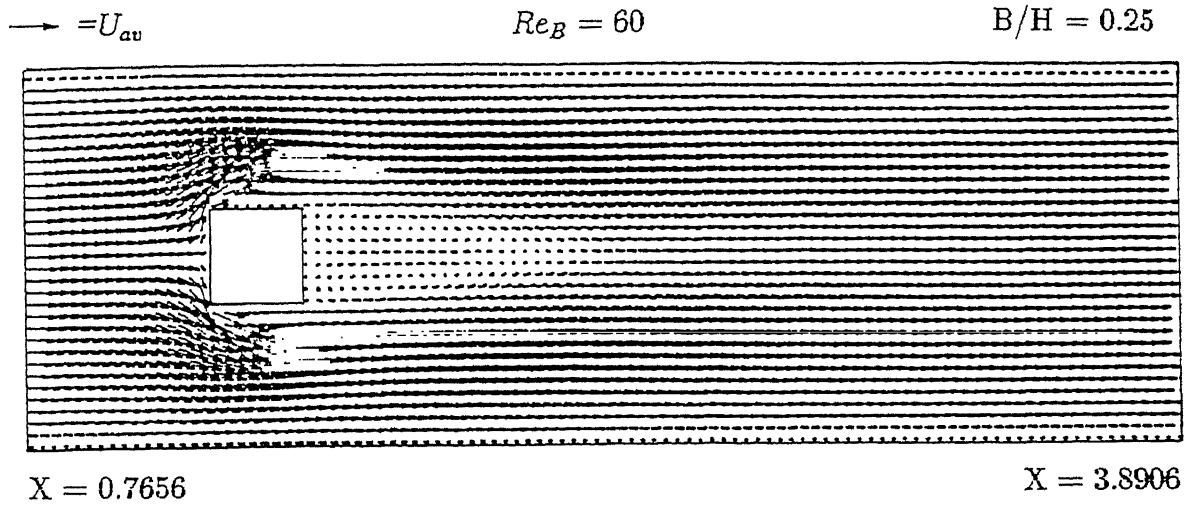
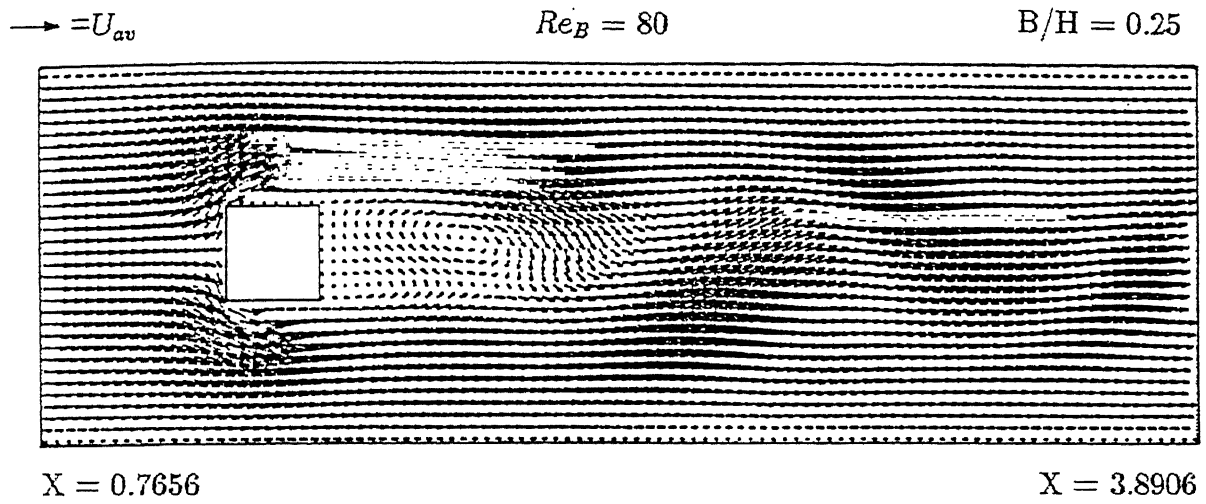
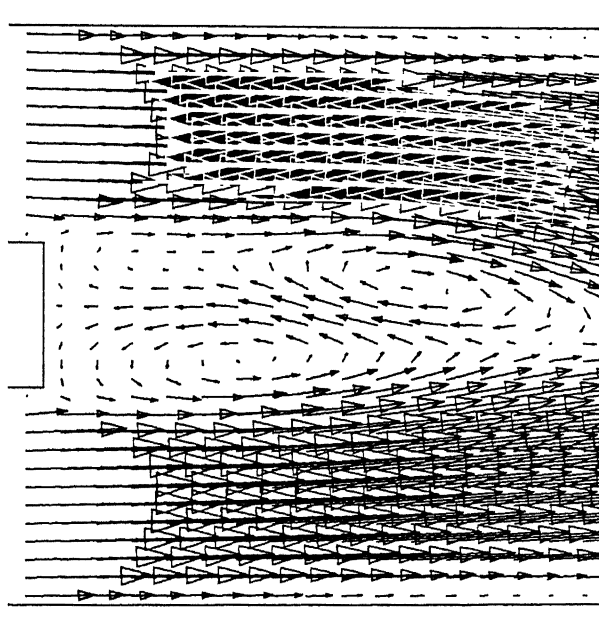


Figure 5.2: Attached vortices behind the obstacle at $Re_B = 60$

tends towards the steady parabolic (not shown in Fig.5.3(a)). For better understanding, a magnified view of the vortices behind the obstacle is shown in the Fig.5.3(b). Okajima (1982) observes the induction of the periodicity in the wake behind a rectangular cylinder in an infinite medium (blockage ratio being negligibly small) at $Re_B = 70$. Davis, Moore and Purtell (1984) finds periodicity in computations with the same geometrical configuration as the present one, at $Re_B \approx 100$. In another numerical investigation, Mukhopadhyay *et al* (1992) observes the critical Reynolds number describing onset of periodicity as 85. Experiments due to Shair *et al* (1963) reveals the critical Reynolds number as 130 for the wake to become periodic in a channel with a circular cylinder in which the blockage ratio is 0.33 and the Reynolds number is defined in terms of a maximum velocity which would exist at the same location as that of the the centre of the cylinder under flow conditions identical with those of the experiment but in absence of the cylinder. It becomes clear that their critical Reynolds number describing the onset of periodicity, based on a definition as ours, would be 87. This is because of the fact that the average velocity is two-thirds of the maximum velocity. The critical Reynolds number obtained by present computation is well within the range of the Reynolds numbers ob-



(a)



(b)

Figure 5.3: (a) The wake is beginning to shed vortices into the stream, $Re_B = 80$
 (b) Magnified view of the wake immediate behind the obstacle

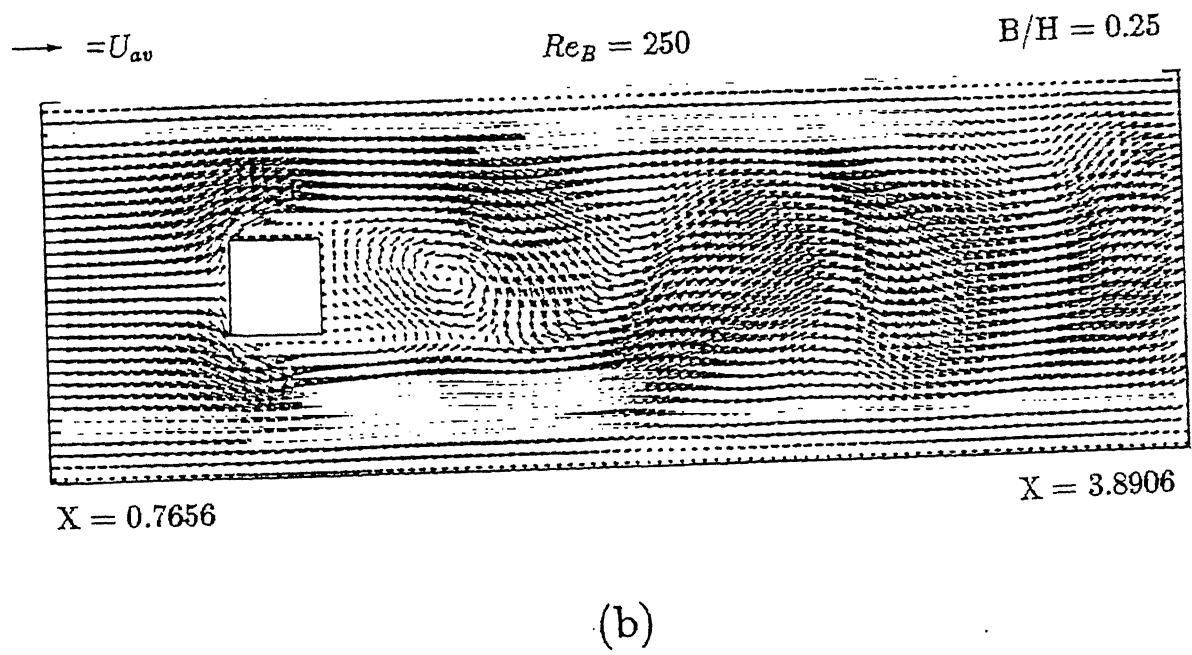
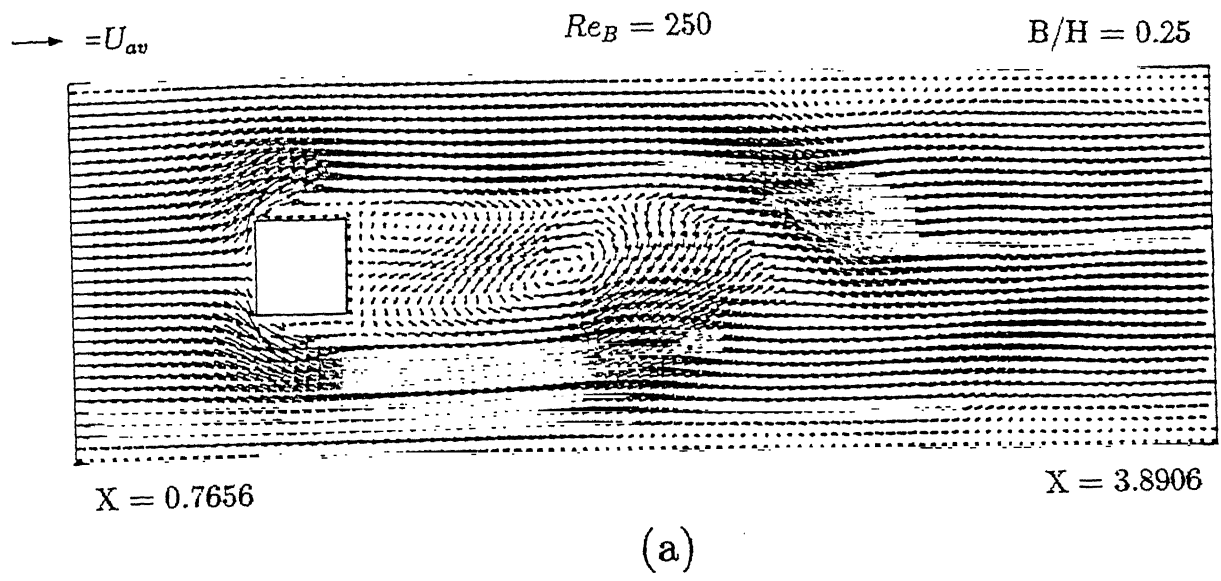


Figure 5.4: Velocity vectors in the channel at different nondimensional time, ($Re_B = 250$) (a) $\tau = 5.0823$ (b) $\tau = 7.4676$

$$Re_B = 375$$

$$B/H = 0.25$$

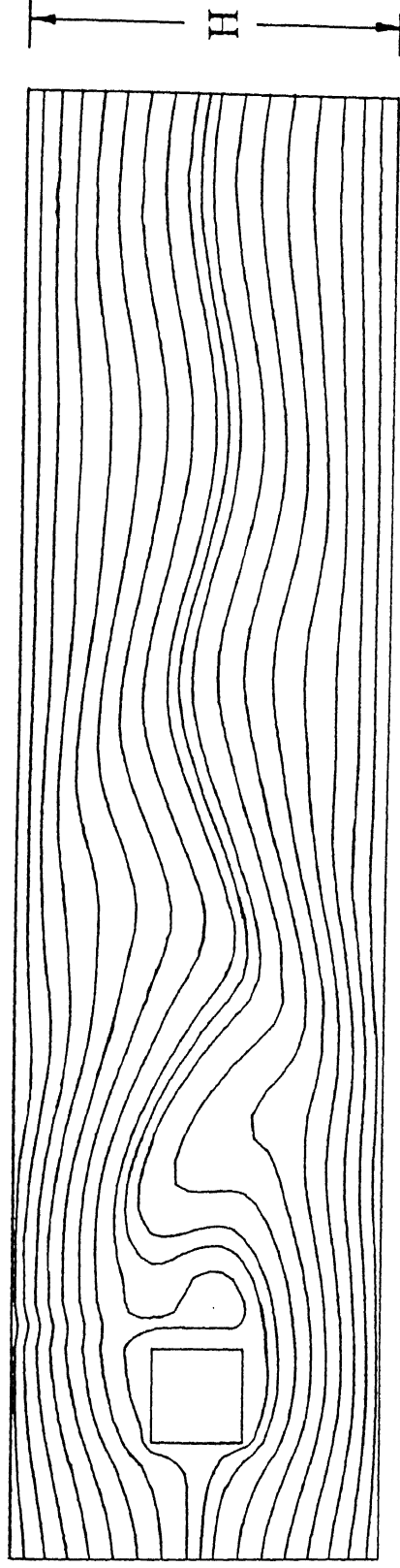


Figure 5.5: Streamline crossing the cylinder in the channel, ($Re_B = 375$)

Obs. No.	$Re_B = \rho U_{av} B / \mu$	B/H	Strouhal Number, S	
			From time-evolution of lift coefficient	From signal traces of fluctuating velocity
1	80	0.125	0.1836	0.1806
2	100	0.125	0.1876	0.1829
3	200	0.125	0.1840	0.1865
4	300	0.125	0.1819	0.1838
5	400	0.125	0.1817	0.1827
6	500	0.125	0.1800	0.1808
7	600	0.125	0.1784	0.1790
8	700	0.125	0.1773	0.1779
9	800	0.125	0.1765	0.1768
10	900	0.125	0.1749	0.1752

Table 5.1: Variation of Strouhal number with Reynolds number

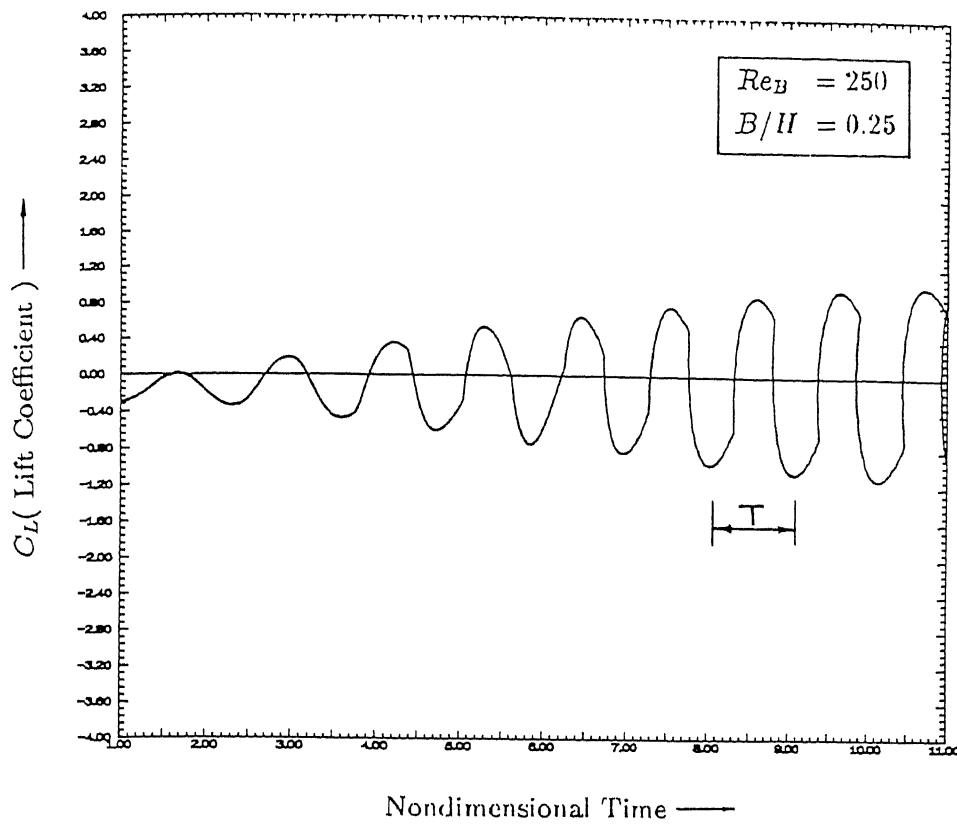
tained by other researchers. Finally, it is worth mentioning that the velocity vector-plots (Figures 5.1, 5.2 and 5.3) are not merely qualitative since the representative scales of the average channel velocity U_{av} are shown in the velocity vector-plots and these can be used for quantitative analysis of the results.

With the increase in Reynolds number beyond the critical one, the von Kármán vortex street is formed and alternate shedding of vortices into the stream becomes prominent (Figures 5.4(a) and 5.4(b)). Figure 5.5 reveals that for a Reynolds number of 375, the flow separates at the leading edge and does not reattach. Needless to say that the entire wake zone undulates like a flag for this Reynolds number. At a low Reynolds number, there is a steady reattachment behind the leading edge and the flow finally separates at the trailing edge which results in symmetrical vortices. But at somewhat higher Reynolds number, after the separation at the leading edge, the flow reattaches either the upper or lower surface of the obstacle during alternate shedding of the vortices into the stream. However, in the range of Reynolds number of 375 the flow remains detached behind the leading edge.

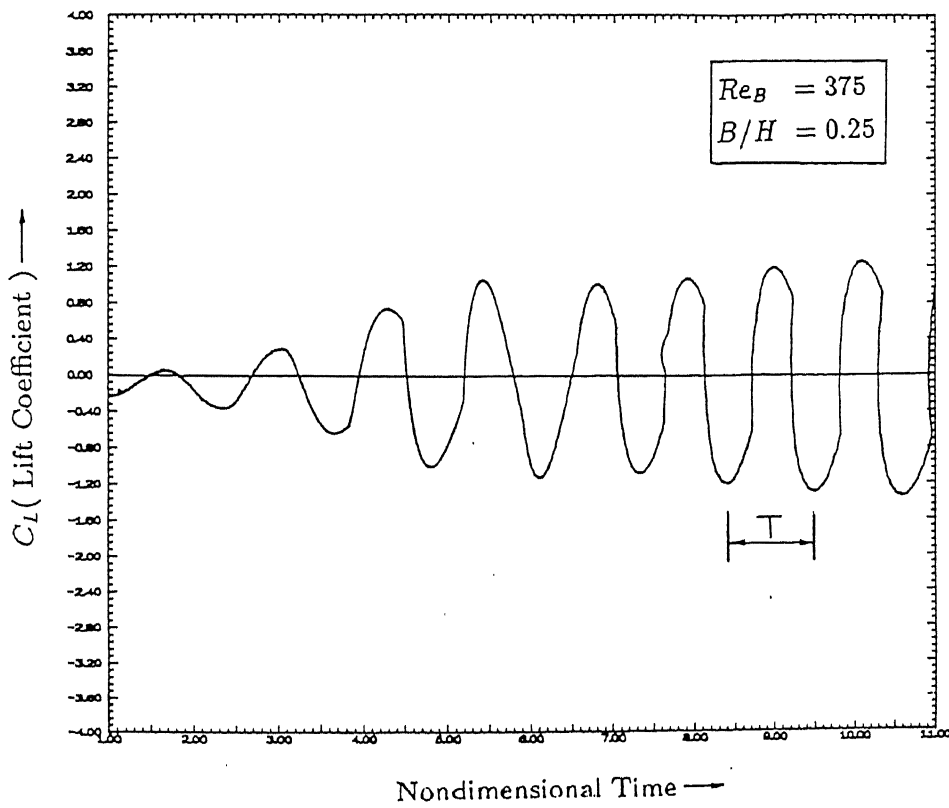
Frequency (f) of vortex shedding has been determined by a technique which borrows some idea from the measurements of Okajima (1982). The normal component of velocity (V -velocity) was recorded at a location which is $3B$ behind the cylinder at the central axis of the channel. In case of steady flow, the flow smoothly divides and reunites around the cylinder, the consequence of which the normal component at that particular location will be zero. But at higher Reynolds number (above the above mentioned critical Reynolds number), the normal velocity keeps fluctuating at the same location. The frequency can be determined from the oscillating signal of the velocity component stored over a fairly long duration of time. Figure 5.6 shows the time evolution of the lift coefficient for two different Reynolds numbers. The vortex shedding frequency can also be determined from the time evolution plot of the lift coefficient distribution. The time period T can be calculated computationally by monitoring the non-dimensional time when the lift coefficient is just crossing the meanvalue. The difference between two such alternative time values (as shown in Fig.5.6(a) and (b)) gives the time period T . Once the time period T is known, the corresponding frequency $f(= 1/T)$ and the Strouhal number $S(= fB/U_{av})$ can also be calculated. It seems from the Figures 5.6(a) and 5.6(b) that the amplitude of the fluctuating coefficients increases with the increase in Reynolds number. Table 5.1 shows the Strouhal number calculations from two methods, namely the signal traces of the fluctuating components and the time-evolution of lift coefficients. The presented data shows agreement between the two values. Table 5.2 compares the Strouhal number variation with the experimental results of Okajima (1982). The present calculation gives somewhat higher Strouhal numbers for the entire range of Reynolds numbers. The discrepancy between the experimental results (Okajima, 1982) and the present results is due to the fact that the experiments were done for a negligibly small blockage ratio. The finite blockage ratio ($B/H = 0.125$) might have brought about some changes in Strouhal number because of the influence of side walls.

5.1.2 Three-Dimensional Flow in a Channel With Built-in Square Cylinder

In three-dimensional flow simulation, $82 \times 26 \times 26$ grid has been used at the finest level. Computations have been done in a channel of length $L/H = 3.333$ with a built-in square



(a)

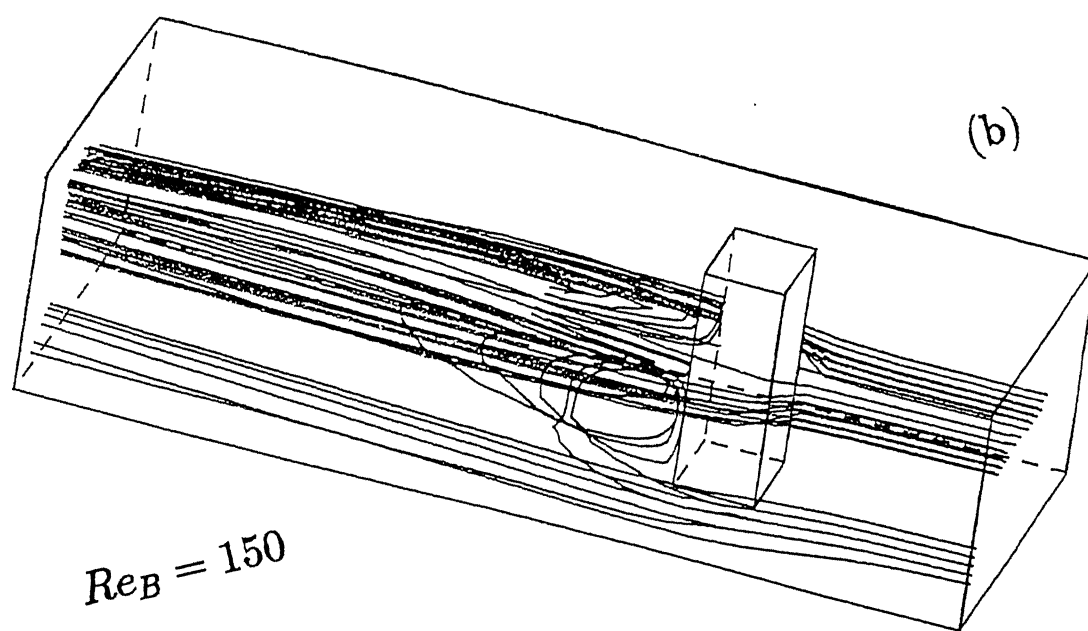
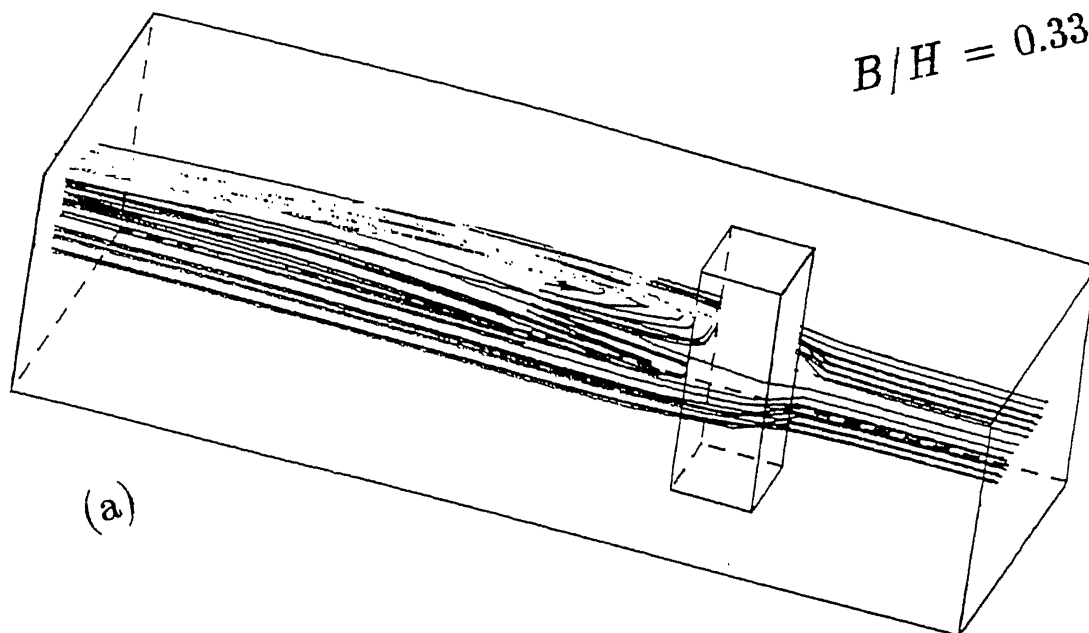


(b)

Figure 5.6: Time evolution of lift coefficient for (a) $Re_B = 250$ (b) $Re_B = 375$

$$Re_B = 150$$

$$B/H = 0.33$$



$$Re_B = 150$$

$$B/H = 0.33$$

Figure 5.7: Pathlines in a channel with built-in square cylinder, $Re_B = 150$

Obs. No.	$Re_B =$ $\rho U_{av} B / \mu$	B/H	Strouhal Number, S	
			Experimental results in infinite medium (Okajima, 1982) (Upper limit)	Numerical prediction in present computation (From signal traces of fluctuating velocity)
1	80	0.125	0.130	0.181
2	100	0.125	0.148	0.183
3	200	0.125	0.150	0.187
4	300	0.125	0.148	0.184
5	400	0.125	0.142	0.183
6	500	0.125	0.139	0.181
7	600	0.125	0.135	0.179
8	700	0.125	0.133	0.178
9	800	0.125	0.130	0.177
10	900	0.125	0.128	0.175

Table 5.2: Comparison of present computation with experimental (Okajima, 1982) results

cylinder of cross sectional area $A \times B$. In this problem, $A/H = B/H = 0.33$ has been used. The obstacle is placed with its geometrical centre at a nondimensional distance $X_R = 1$ from the inlet. The channel and obstacle axes are aligned. The height of the obstacle is same as that of the channel. Only one blockage ratio, viz, 0.33 is used for this simulation.

In Fig.5.7(a), the particle traces in a channel for a low Reynolds number flow $Re_B = 150$ are shown. The plotted lines are the pathlines showing the way of fluid particles through the channel beginning at various starting points. This plot can be depicted as the numerical flow visualization. Under steady state, these lines are streamlines. However, in Fig.5.7(a), the structure of wake in the immediate neighbourhood of the horizontal symmetric plane is nearly the same as two-dimensional flows.

However, in another view (Fig.5.7(b)) between the plane of symmetry and the

bottom wall, a screw-like helical structure of flow is observed. As such, Fig.5.7(b) explains the formation of a horseshoe vortex system. As fluid approaches the stagnation line of a square obstacle in cross flow, it slows down and its pressure increases. The smaller velocity in the boundary layer on the flat bottom plate which supports the square cylinder leads to a smaller pressure increase. Thus the induced pressure gradient causes a flow towards the bottom wall which interacts with the main-stream. The fluid rolls up forming vortices which are finally swept around the obstacle base, and are carried downstream.

5.2 Computational Aspects of the Multigrid Technique

In this section, the performance of the multigrid algorithm for both the two-dimensional and the three-dimensional flow situation with built-in square obstacle is presented. In order to assess the behaviour of the algorithm critically, several calculations with variation in the Reynolds number have been made for each of the flow situation. Since the multigrid strategy has been applied only to pressure-velocity equation, the results of the single-grid and multigrid should be the same. It has been observed from the velocity-vector plots that both the results are in good agreement with respect to their quantitative and qualitative measures. It is well known that the relaxation factor has its significant role in the convergence of solution. In single-grid calculation this factor is chosen as 1.8. But for the multigrid computation, special care has to be taken in choosing the relaxation factor. Successive over-relaxation has not been used as the smoothing operator. The over-relaxation destroys the high-frequency smoothing that is so crucial for the multigrid method. In our present calculation a fixed relaxation factor is used equal to one.

5.2.1 Two-Dimensional Case

For the computation with the multigrid technique, grid size of 314×66 has been used as the finest grid. The number of grid level is restricted by obstacle size. However, we have computed for three number of grid levels with the boundary conditions in every grid levels. In Chapter-4, we have already mentioned about the interpolation of values

Re_B $= \rho U_{av} B / \mu$		CPU Times Hr : Min : Sec	Workunits to get converged steady solution	Amount of work in relation to single grid
25	Multigrid	1:10:46.4	10017	11.98 %
	Single-grid	2:05:17.9	83629	
40	Multigrid	1:18:31.0	11199	12.45 %
	Single-grid	2:13:22.3	89950	
50	Multigrid	2:10:31.2	20478	17.76 %
	Single-grid	3:17:45.0	115306	

Table 5.3: Comparison of CPU-times and Workunits between the multigrid and single-grid for two-dimensional problem

near the boundary where the general prolongation rule does not hold good. But in our present calculation, we have made the prolongation routine in such a way that it does not require any linear extrapolation of inner values to get the boundary values.

The present computation has been performed on a HP 9000/735 series computer. The system has 144 MB of RAM, 2×1 GB and 2×2 GB of Hard Disk and 40 Mflops (scalar) peak performance.

The performance of multigrid technique is assessed by observing the two parameters, namely, Central Possessing Unit (CPU) time and the Workunit. The Workunit is defined as the one relaxation sweep on the finest grid level. Table 5.3 shows the CPU times and the Workunits for one gridsize (314×66) and different Reynolds numbers for steady flow. In the present computation, we have recorded the total number of relaxation sweeps (total Workunits) in the finest grid level for multigrid as well as for the single-grid till the solution is converged. Comparison of both the treatments shows that the multigrid requires very less number of relaxation sweeps (on finest grid level) compared to single-grid. The CPU time for the multigrid varies in the range of 50 - 65 % of single-grid time. The saving in computational time due to the multigrid is about 35 - 50 % in comparison to single-grid for different Reynolds numbers.

The reduction of work obtained by the multigrid treatment depends on the amount

Re_B $= \rho U_{av} B / \mu$		Workunits to get converged steady solution	Amount of work in relation to single grid
33	Multigrid	4239	37.77 %
	Single-grid	11223	
50	Multigrid	4974	39.65 %
	Single-grid	12545	
70	Multigrid	5712	40.08 %
	Single-grid	14253	
100	Multigrid	7317	41.67 %
	Single-grid	17560	

Table 5.4: Comparison of Workunits between the multigrid and single-grid for the three-dimensional problem

of work for the corresponding single-grid computation of the continuity equation, since the amount of work for the momentum equation remains unchanged. The higher the fraction of the work for the continuity equation in comparison to the whole work, the higher is the reduction of the work achieved by the multigrid treatment. Our computational tests with multigrid show a reduction of about 80 - 90 % of work for a blockage ratio of 0.25 depending on the Reynolds numbers.

For the unsteady flows, we observed that for the multigrid calculation, the periodicity is set in the flow field at the expense of much less CPU time as compared to the single-grid calculations.

5.2.2 Three-Dimensional Case

In the multigrid treatment, the finest grid size is as the single-grid ($82 \times 26 \times 26$) for three-dimensional flows. Three grid levels have been deployed for computation. In Chapter-4, it has already been mentioned that for adaptive cycling, the switching factor δ_v is chosen as 0.6. This particular value can be varied from problem to problem. For the two-dimensional case, stated in the previous section, δ_v equal to 0.6 gives good

convergence rate but for the present configuration of interest, *i.e.*, for a three-dimensional channel-flow, the optimum value is found to be 0.3. The other treatments concerning the operations of the multigrid technique have already stated in Chapter-4.

The performance of the multigrid technique is not found very exciting in the three-dimensional case. The performance of the multigrid treatment basically depends on the type of errors that to be smoothened during relaxation. For the three-dimensional problem, it has been observed that the low frequency errors are smoothened out very quickly and only for the first two or three time steps it takes large number of relaxation sweeps on pressure-velocity equation to make the flow field divergence free. After the solution smoothened out in two to three time steps, successive time steps need only five to seven relaxation sweeps to make al the cells divergence free. In the multigrid method, every V-cycle needs atleast three sweeps in the finest level. However, some enhancement in computation speed has been observed for the multigrid calculations. Table 5.4 shows the comparison of Workunits between the multigrid and the single-grid calculations for the steady flow cases.

Chapter 6

Concluding Remarks

Full Navier-Stokes equations have been solved for two and three-dimensional flows in a channel with a built-in square cylinder. Vortex shedding behind the square cylinder induces periodicity in the flow field. Details of the phenomenon are simulated through numerical flow visualization. Computations for three-dimensional flow show formation of horseshoe vortices in the wake of the square obstacle. The periodicity of the flow is characterized by the nondimensional frequency known as Strouhal number.

A V-cycle multigrid technique has been suitably adapted to accelerate the speed of convergence of the solution. The multigrid technique improves the computation time significantly. However, for two-dimensional flows the multigrid technique appears to be more effective as compared to three-dimensional cases. For three-dimensional calculations, the convergence becomes slow after the removal of high frequency errors.

References

1. Agarwal, R. K., Unigrid and Multigrid Algorithms for The Solution of Coupled, Partial-differential Equations Using Fourth-order-accurate Compact Differencing, rept. MDRL - 81 - 35, McDonnell Douglas Research Laboratories, St. Louis, MO, 1981.
2. Brandt, A., Multigrid techniques: 1984 guide with applications to fluid dynamics, Lecture Series 1984 - 04, von Kármán Institute, 1984.
3. Brandt, A., Dendy, J. E., and Ruppel, H., The Multigrid Method for Semi-Implicit Hydrodynamic Codes, *Journal of Comp. Phys.*, vol. 34, pp. 348 - 370, 1980.
4. Brockmeier, U., Mitra, N. K., and Fiebig, M., Multigrid Marker-And-Cell (SOLA) Algorithm for Three Dimensional Flow Computation, *Proc. of The Sixth GAMM - Conference on Numerical Methods in Fluid Mechanics*, pp. 23 - 30, 1986.
5. Chima, R. V., and Johnson, G. M., Efficient solution of The Euler and Navier-Stokes equations with a vectorized multiple-grid algorithm, *AIAA J.*, vol. 23, Part 1, pp. 23 - 32, 1985.
6. Chorin, A. J., A Numerical Method for Solving Incompressible Viscous Flow Problems, *Journal of Comp. Phys.*, vol. 2, pp. 12 - 26, 1967.
7. Davis, R. W., Moore, E. F., and Purtell, P., A Numerical and Experimental Study of Confined Flows Around Rectangular Cylinders, *Phys. Fluids*, vol. 27, pp. 46 - 59, 1984.
8. Fuchs, L., and Zhao, H. S., Solution of three-dimensional viscous incompressible flows by a multigrid method, *Int. J. Numer. Methods Fluids*, vol. 4, pp. 539 - 555, 1984.
9. Galpin, P. F., Van Doormal, J. P., and Raithby, G. D., Solution of The incompressible mass and momentum equations by application of a coupled equation line solver, *Int. J. Numer. Methods Fluids*, vol. 5 pp. 615 - 625, 1985.

10. Ghia, U., Ghia, K. N., and Shin, C. T., High - Re Solutions for Incompressible Flows Using The Navier - Stokes Equations and a Multigrid Method, *Journal of Comput. Phys.*, vol. 48, pp. 387 - 411, 1982.
11. Hackbusch, W.; Trottenberg, U.(Ed.):
Multigrid Methods,
Proc. of The Conference Held at Köln - Porz, November 23rd - 27th, 1981. Lecture Notes in Mathematics, 960, Springer - Verlag, Berlin, 1982.
12. Harlow, F. H., and Welch, J. E., Numerical Calculation of Time-Dependent Viscous Incompressible Flow of Fluid with Free Surfaces, *The Physics of Fluids*, vol. 8, pp. 2182 - 2188, 1965.
13. Hirt, C. W., and Cook, J. L., Calculating Three Dimensional Flows Around Structures and Over Rough Terrain, *Journal of Comp. Phys.*, vol. 10, pp. 324 - 340, 1972.
14. Hirt, C. W., Nichols, B. D., and Romero, N. C., SOLA - A Numerical Solution Algorithm for Transient Fluid Flows, *LA - 5852, Los Alamos Scientific Laboratory Report*, 1975.
15. Jameson, A., Solution of The Euler equations by multigrid methods, *Appl. Math. Comput.*, vol. 13, pp. 327 - 356, 1983.
16. Kiehlm, P., Mitra, N. K., and Fiebig, M., Numerical Investigation of Two- and Three-Dimensional Confined Wakes Behind A Circular Cylinder in A Channel, AIAA, 24th Aerospace Sciences Meeting, 1986.
17. Mukhopadhyay, A., Biswas, G., and Sunderarajan, T., Numerical Investigation of Confined Wakes Behind a Square Cylinder in a Channel, *Int. J. Numer. Methods Fluids*, vol. 14, pp. 1473 - 1484, 1992.
18. Okajima, A., Strouhal Numbers of Rectangular Cylinders, *J. Fluid Mech.*, vol. 123, pp. 379 - 398, 1982.
19. Peyret, R., and Taylor, T. D., Computational Methods for Fluids Flow, Springer-Verlag, New York, 1983.

20. Phillips, R. E., Miller, T. F., and Schmidt, F. W., A multilevel - multigrid algorithm for axisymmetric recirculating flows, in: Proc. 5th Turbulent Shear Flows Conference, Cornell University, Ithaca, NY, 1985.
21. Phillips, R. E., and Schmidt, F. W., A Multilevel - Multigrid Technique for Recirculating Flows, *Numerical Heat Transfer*, vol. 8, pp. 573 - 594, 1985.
22. Shair, F. H., Grove, A. S., Petersen, E. E., and Acrivos, A., The Effect of Confining Walls on The Stability of The Steady Wake Behind a Circular Cylinder, *J. Fluid Mech.*, vol. 17, pp. 546 - 550, 1963.
23. Stüben and Trottenberg, U., Multigrid methods, fundamental algorithm, model analysis and applications, in: Hackbusch, W., and Trottenberg, eds., Multigrid Methods, Lecture Notes in Mathematics 960 (Springer, Berlin, 1982) pp. 1 - 176.
24. Vanka, S. P., Block-implicit calculation of steady turbulent recirculating flows, *Int. J. Heat Mass Transfer*, vol. 28, part 11 ,pp. 2093 - 2103, 1985.
25. Vanka, S. P., A calculation procedure for three-dimensional recirculating flows, *Comput. Meths. Appl. Mech. Engrg.*, vol. 55, pp. 321 - 338, 1986a.
26. Vanka, S. P., Block - Implicit Multigrid Calculation of Two Dimensional Recirculating Flows, *Comput. Meths. Appl. Mech. And Engrg.*, vol. 59, pp. 29 - 48, 1986b.
27. Vanka, S. P., Block-implicit multigrid solution of Navier-Stokes equations in primitive variables, *Journal of compt. phys.*, vol. 65, pp. 138 - 158, 1986c.
28. Vanka, S. P., Calculation of axisymmetric turbulent confined diffusion flames, *AIAA J.*, vol. 24, Part 3, pp. 462 - 469, 1986d.
29. Vieceilli J. A., A Computing Method for Incompressible Flows Bounded by Moving Walls, *Journal of Comp. Phys.*, vol. 8, pp. 119 - 143, 1971.
30. Zedan, M., and Schneider, G. E., A coupled strongly implicit procedure for velocity and pressure computation in fluid flow problems, *Numerical Heat Transfer*, vol. 8, Part 5, pp. 537 - 558, 1985.